

PAPER



Cite this: *J. Mater. Chem. A*, 2018, 6, 231

Enhancing the real-time detection of phase changes in lithium–graphite intercalated compounds through derivative operando (dOp) NMR cyclic voltammetry†

Jose L. Lorie Lopez,  Philip J. Grandinetti * and Anne C. Co *

Robust and reliable diagnostic tools that can be employed under operating conditions are crucial to understanding performance and failure mechanisms in battery processes. The operando spectrum of a battery often consists of a strongly overlapping mixture of time dependent and independent resonances due to the compositional complexity. Here we report a new method called derivative operando (dOp) that improves the resolution of operando nuclear magnetic resonance (NMR) spectra by removing time independent signals and further distinguishes between time dependent signals associated with the formation and removal of species. This approach not only provides better resolution but also more clearly reveals correlations between resonances and the chemical transformations occurring at a specific potential. With the dOp-NMR method we detect the formation of lithium graphite intercalation compounds (GICs), including the signatures of LiC_{72} and its precursors, which have been previously undetected. We also observe a clear correlation of the dOp ^7Li NMR spectra of lithium metal dendrites on the counter electrode with the chemistry of the working electrode.

Received 25th August 2017
Accepted 27th November 2017

DOI: 10.1039/c7ta07521a

rsc.li/materials-a

1 Introduction

The growing demand for batteries with higher energy and power densities has stimulated considerable efforts towards the development of new materials.^{1–3} Concurrently, advances in robust, non-destructive *in situ* and operando characterization techniques⁴ are becoming critical as we attempt to improve our understanding of how structural transformations, reaction dynamics, and transient non-equilibrium processes at various length and time scales determine battery performance and failure mechanisms. A number of complementary operando techniques have been developed to probe specific chemical processes, each with its respective advantages and limitations. For instance, operando X-ray scattering^{5–7} has been invaluable for identifying and detecting transformations among various crystalline phases during cycling. Another example is operando scanning probe microscopy,⁸ which monitors the expansion and contraction of electrode materials. Neutron depth profiling^{9–13} has been used to quantify lithium accumulation/depletion, lithium rearrangement, and lithium transport during lithiation and delithiation processes in lithium ion batteries. Nuclear magnetic resonance (NMR) spectroscopy and imaging (MRI), in particular, have become important new

tools in operando studies of battery materials using NMR active nuclei to provide quantitative identification of structural species in crystalline and non-crystalline solids as well as in fluid phases, including anode materials,^{14–16} metallic dendrites,¹⁷ electrolytes,¹⁸ and electrolyte decomposition products.¹⁹

In spite of these successes, the interpretation and assignment of an operando signal from a battery is challenging due to overlapping signals arising from the electrolyte, cathode, anode, and solid–electrolyte interface (SEI) phases. In the case of NMR the higher spectral resolution of magic-angle spinning (MAS) has remained out of reach due to a number of technical hurdles, notably the magnetic braking due to eddy currents arising in metallic current collectors as well as in metallic electrode materials during sample rotation.

Reported herein is an NMR method we have developed that (1) improves the resolution of overlapping resonances – aiding in spectral assignments – and more importantly, (2) differentiates the signals due to the formation and removal of species by eliminating all signals that are constant during the battery processes through signal processing. This approach, which we have coined “derivative operando” (dOp) spectroscopy, is not limited to processing NMR spectra but can be generally applied to other operando methods to remove sizable signals that remain invariant during the operando process. The dOp spectrum not only provides better resolution but also offers a more direct correlation of the species formed and removed with the electrochemical current measured at each potential/time.

Department of Chemistry and Biochemistry, Ohio State University, USA. E-mail: grandinetti.1@osu.edu; co.5@osu.edu

† Electronic supplementary information (ESI) available. See DOI: 10.1039/c7ta07521a

2 Methods

2.1 Sample preparation

2.1.1 Graphitic carbon electrode preparation. A slurry was made from 85 wt% mesocarbon microbeads (MCMB) (TB-17, MTI Corp.) with 5 wt% carbon black (Carbon Vulcan Black XC-72R) and 10 wt% polyvinylidene fluoride (PVDF, MTI Corp.) in *N*-methylpyrrolidone (NMP, MTI Corp.). The slurry was cast on a thin copper foil (9 μm thick, MTI Corp.) current collector using an adjustable doctor blade (MSK-AFA I, MTI Corp.) set at a thickness of 0.4 mm followed by drying from 65 $^{\circ}\text{C}$ to 90 $^{\circ}\text{C}$ for 4 hours with intermittent vacuum. The electrodes were cut, weighed, and vacuum dried before assembling the battery. Each dry electrode contained around 9 mg of active material.

2.1.2 Electrochemical cell. A modified version of the bag cell battery configuration developed by Bellcore²⁰ was used in this study. A two-electrode battery half-cell was assembled in an Ar filled glove box (mBraun) with continuous detection of H_2O (<0.5 ppm) and O_2 (<0.5 ppm). The carbon electrode served as the working electrode and a high purity lithium metal foil (0.3 mm thick, Chemetall Foote Corp.) served as the combined counter and reference electrode. A 1 M solution of lithium hexafluorophosphate (LiPF_6) in a 1 : 1 volume ratio of ethyl carbonate (EC) and dimethyl carbonate (DMC) was used as the electrolyte (Purolite A5 Series, Novolyte Technologies). The carbon and Li electrodes were separated by a Celgard[®] 2400 separator soaked in the electrolyte prior to assembly. The lithium electrode was pressed onto a copper mesh current collector. The cell configuration was similar to that shown by Letellier *et al.*,²¹ but two working electrodes were used to increase the NMR signal as illustrated in Fig. 1A. The stack was vacuum sealed in a polyethylene plastic bag inside the glove box. The electrochemical cell was 8 mm wide and 10 mm long and contained a total of 18.1 mg of MCMB.

The data presented here were measured using the same carbon electrode. We have done this to ensure consistency in our comparison of NMR and electrochemical data. We have

repeated all experiments reported here with several identical carbon electrode systems to confirm that all the trends reported are statistically significant and reproducible.

2.2 NMR measurements

NMR measurements were performed on a hybrid Tecmag Apollo-Chemagnetics CMX II 9.4 T (155.48 MHz for ^7Li) NMR spectrometer. All frequency shifts are given in terms of the dimensionless quantity,

$$\delta = \frac{\nu - \nu_{\text{ref}}}{\nu_{\text{ref}}}, \quad (1)$$

where ν_{ref} corresponds to an external ^7Li NMR resonance reference frequency from 1 M LiCl. The inversion recovery sequence²² was used for all measurements of spin-lattice relaxation times, T_1 . The NMR T_1 relaxation times and spin coupling parameters for lithiated graphite sites detected in this study are given in Table 1 along with the potential at which they are formed. All measurements were performed at ambient temperature.

The ^7Li nucleus has spin $S = 3/2$ and has three NMR active transitions: the central transition $m_s = \frac{1}{2} \rightarrow -\frac{1}{2}$ and two satellite transitions, $m_s = \frac{3}{2} \rightarrow \frac{1}{2}$ and $m_s = -\frac{1}{2} \rightarrow -\frac{3}{2}$. In addition to having a nuclear magnetic dipole moment, the ^7Li nucleus also has an electric quadrupole moment. The coupling between this quadrupole moment and local electric field gradients can lead to an anisotropic broadening of the satellite transition resonances as illustrated in Fig. 2A. These line shapes can appear somewhat distorted with intensity loss from the broad component of the anisotropic line shape due to receiver dead time at the beginning of signal acquisition. In contrast, the central transition experiences no anisotropic quadrupolar broadening to first order.²³

Radio frequency power levels were reduced to 25 watts to eliminate arcing in the coil. This corresponds to a rf field strength of $\omega_1/(2\pi) = 14.4$ kHz. At this power, nutation experiments show that the lithium metal resonance nutates at twice the rate of the lithium sites in the electrolyte and the graphite intercalated compounds (GICs). An increase by a factor of $(S + 1/2)$ in the nutation frequency (2 for ^7Li) indicates that the rf pulse excites only the central transition of the Li metal resonance due to its larger quadrupole splitting $\omega_q \gg \omega_1$. This observation of faster nutation of the lithium metal resonance conflicts with the conclusion of Chevallier *et al.*¹⁶ who noted that the lithium nuclei in the metal experience no electric field gradient. At this power a 2.5 μs pulse length corresponds to a 13 $^{\circ}$ rotation of all lithium transitions for sites in the electrolyte and GICs and a 26 $^{\circ}$ rotation of the central transition for sites in the lithium metal.

Fig. 2B shows a typical *in situ* ^7Li NMR spectrum of the Li ion cell with a lithium counter electrode and graphite as the working electrode at a potential where LiC_6 is the dominant form of lithiated graphite. The ^7Li NMR resonance at $\delta = 274$ ppm is assigned to the central transition of ^7Li in the metallic lithium counter electrode. The ^7Li satellite transitions

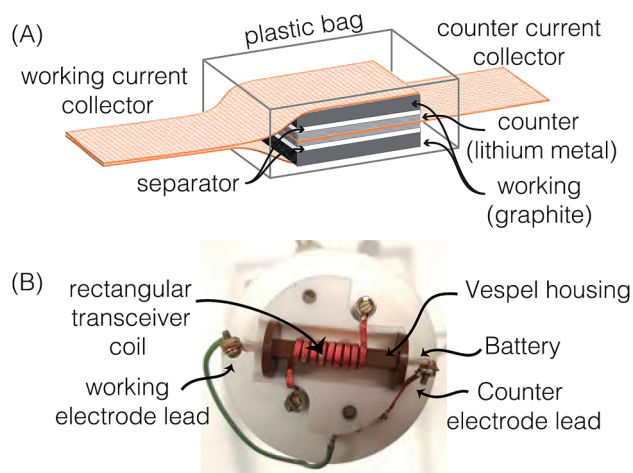


Fig. 1 (A) Schematic drawing of a bag cell configuration with two working electrodes. (B) Labeled photo of the modified probe head with a rectangular coil and Vespel housing.

Table 1 ^7Li NMR shifts, quadrupole coupling parameters, relaxation times, fraction of transverse magnetization, predicted integrated signal intensity based on reaction stoichiometry for the GICs found in this work. The quadrupole asymmetry parameter is approximately $\eta_q = 0$ for all sites

Li site	Stage	Potential/V (vs. Li/Li^+)	$\delta_{\text{Li}}/\text{ppm}$	C_q/kHz	T_1/s	Fraction of transverse magnetization	Predicted integrated intensity
Li metal	—	—	274	—	0.140	0.369	—
Precursors	>8	>0.47	~ -82 to -2.5	—	—	—	—
LiC_{72}	8	0.47	-2.5 to -1.0	—	—	—	—
LiC_{36}	4	0.189	~ 2	36	3.15	0.096	0.2889
LiC_{27}	3	0.137	6.3	36	3.87	0.085	0.1702
LiC_{18}	2L	0.116	12.5	36	—	—	—
LiC_{12}	2	0.086	48.3	34	2.14	0.118	0.7074
LiC_6	1	0.047	45.2	44	1.80	0.128	2.2968

in the metal are too broad for detection. The strongly positive shift from 0 ppm arises from an increased magnetic field at the nucleus due to an interaction with the conduction electrons called the Knight shift.²⁴ The lithium metal sites have a spin-lattice relaxation time of $T_1 = 140$ ms. The electrolyte, LiPF_6 , and SEI appear around -2.5 ppm. As noted earlier these resonances nutate at a rate of ω_1 . The additional lack of any observable anisotropic broadening indicates that these ^7Li sites experience little to no quadrupolar coupling to local electric field gradients as would be expected for a Li^+ cation in an isotropic environment. The ^7Li spin-lattice relaxation time of

LiPF_6 is 675 ms. Most notably, seen in this spectrum are central and satellite transitions for ^7Li of LiC_6 . The central transition peaks at approximately 45 ppm. The quadrupolar coupling—responsible for the anisotropic broadening of the satellite transitions—is characterized by a constant of $C_q = 44$ kHz and quadrupole asymmetry parameter of approximately $\eta_q = 0$. The ^7Li spin-lattice relaxation time of LiC_6 is 1.8 s. Finally, we note that the lower intensity resonance at approximately 18 ppm is assigned to lithium naphthalenide which is produced during the formation of LiC_{12} .

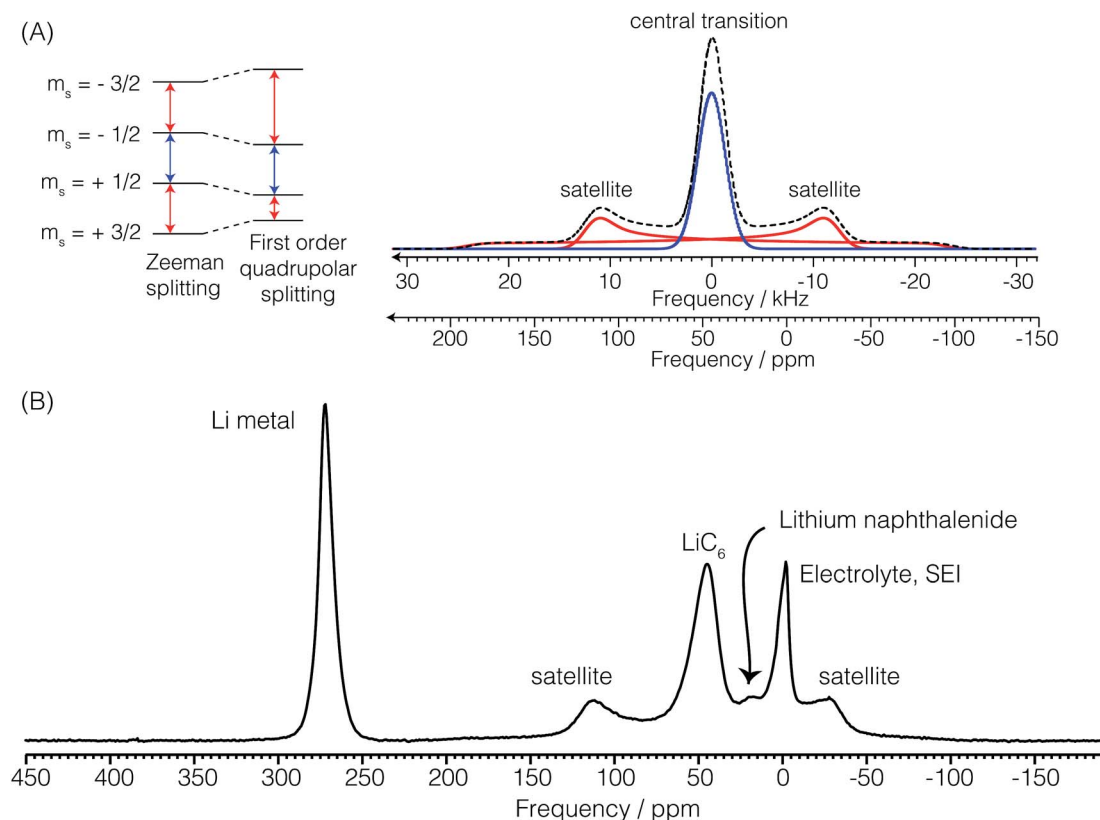


Fig. 2 (A) Component and overall powder pattern NMR line shapes for the two satellite transitions and the central transition of the ^7Li nucleus with a quadrupolar coupling constant of $C_q = 44$ kHz and a quadrupolar asymmetry parameter of zero. (B) *In situ* ^7Li NMR spectrum of the cell during the formation of LiC_6 showing the resonant frequencies of the lithium metal, electrolyte and SEI, lithium naphthalenide, and the quadrupolar powder pattern of LiC_6 .

2.2.1 Operando study. The electrochemical bag cell was placed inside a thin (0.635 mm thick) wall rectangular Vespel housing, as shown in Fig. 1B. The thickness of the battery was matched to the opening of the housing and Teflon shims were added above and below the cell to keep a uniform pressure applied across the cell and maintain electrical contact. A nine turn rectangular (20 mm × 5 mm × 14 mm) transceiver coil was wrapped around the rectangular Vespel housing and mounted on a Bruker static probe as also shown in Fig. 1B. The housing was oriented in order to place the electrode face parallel to B_0 in order to minimize magnetic susceptibility broadening.²⁵ The probe was modified to bring the potentiostat wires up through the base of the probe to maintain a common ground with the probe circuit. Low pass filters were connected in line with the potentiostat cables to block high frequency noise injected from the potentiostat and stray pick up of the potentiostat cables from reaching the NMR receiver coil.

A CHI760D (CH Instruments, Inc., Austin, TX) galvanostat/potentiostat was used to perform the electrochemical measurements. All voltages were measured and reported against Li/Li^+ . The initial open circuit potential (OCP) of the cell was approximately 3.1 V vs. Li/Li^+ . The OCP was measured over a period of 15 minutes to ensure steady state potential before the beginning of the operando measurements. The NMR signal was simultaneously acquired with three cyclic voltammograms (CV) between 700 and 5 mV at a potential sweep of $2 \mu\text{V s}^{-1}$.

For operando NMR/cyclic voltammetry experiments the acquisition time of a single free induction decay was 10.24 ms. With a 13° pulse and a T_1 of 1.8 s for the LiC_6 we set the recycle delay time to 49.4 ms to optimize sensitivity according to the Ernst angle equation²⁶ and averaged 15 084 scans for each spectrum. Because of the differential ^7Li relaxation times of the GICs we calculate and present in Table 1 the fraction of transverse magnetization after the steady state has been reached for the excitation pulse length and recycle delay used in the operando NMR measurements. A fraction of 1 corresponds to the excitation of equilibrium magnetization. There is a systematic decrease in ^7Li T_1 with increasing lithiation of the GICs leading to a slight but not insignificant loss in GIC resonance intensity (quantitative areas) with decreasing lithiation.

With these parameters each spectrum was acquired in $\Delta t_{\text{op}} = 15$ min giving an electrochemical resolution of 1.8 mV per NMR spectra. A total of $N_{\text{op}} = 2317$ spectra were acquired for a total measurement (operando) time, t_{op} , of 580 h (approx. 24 days).

2.2.2 Signal processing. The initial phase of the NMR signal varied during the operando experiment while the potentiostat varied the voltage and current through the electrochemical cell. A zeroth-order phase correction was applied to each of the N_{op} free induction decays by adjusting the maximum signal amplitude at $t = 0$ to be in the real part, where t is the acquisition time in the NMR experiment. Additional zeroth and first-order phase corrections were applied identically to all $N_{\text{op}} = 2317$ spectra. All signal processing was performed with the program RMN.²⁷

The derivative of the operando signal as a function of operando time, t_{op} , and NMR transition frequency, ω , is calculated via the Fourier derivative theorem which states

$$\text{if } f(t_{\text{op}}, \omega) = \int_{-\infty}^{\infty} a(\omega_{\text{op}}, \omega) e^{i\omega_{\text{op}} t_{\text{op}}} dt_{\text{op}},$$

$$\text{then } \frac{d}{dt_{\text{op}}} f(t_{\text{op}}, \omega) = \int_{-\infty}^{\infty} i\omega_{\text{op}} a(\omega_{\text{op}}, \omega) e^{i\omega_{\text{op}} t_{\text{op}}} dt_{\text{op}}. \quad (2)$$

In other words, the derivative of the signal, $f(t_{\text{op}}, \omega)$, is a convolution of the signal with the inverse Fourier transform of the function $i\omega_{\text{op}}$. This function, however, will amplify high frequency noise so a Hamming function is applied to cut off the undesired higher frequencies. In practice this is implemented in four steps: (1) application of a discrete N_{op} point Fourier transform of the signal with respect to the battery operando time, t_{op} ; (2) multiplication of the signal by $i\omega_{\text{op}}$; (3) multiplication of the signal by a Hamming function given by

$$g(\omega_{\text{op}}) = \begin{cases} \alpha + \beta \cos\left(\frac{\omega_{\text{op}}}{2\nu_c}\right), & \text{for } |\omega_{\text{op}}| \leq 2\pi\nu_c, \\ 0, & \text{for } |\omega_{\text{op}}| > 2\pi\nu_c, \end{cases} \quad (3)$$

where ν_c is the cutoff frequency—in this case set to $150 \mu\text{Hz}$ —and $\alpha = 0.54$ and $\beta = 0.46$ are predefined constants for the Hamming function; and (4) application of a discrete inverse Fourier transform with respect to ω_{op} to obtain the derivative signal with respect to the battery operando time. A more detailed step-by-step guide in the derivative processing of the signal is given in Section S2 of the ESI.†

3 Results and discussion

3.1 Cyclic voltammetry

Fig. 3A shows the cyclic voltammogram of the carbon electrode measured at a sweep rate of $2 \mu\text{V s}^{-1}$ from 700 to 5 mV vs. Li/Li^+ . The direction of the scan is indicated in the figure. Negative currents indicate lithiation or reduction and positive currents indicate delithiation or oxidation processes. The peak assignments were based on *in situ* XRD measurements.^{5,7} The first cycle (blue dashed line) shows broader and shifted peaks as the freshly prepared battery is negatively polarized. A solid electrolyte interface (SEI) slowly forms on the surface of both electrodes, changing their surface chemistry, and therefore, resulting in a broader distribution of potentials that shift with respect to each other. As the electrode gets passivated, the potential of the lithium anode reaches a steady state, and the observed peak potentials for the subsequent cycles on lithium do not change substantially, reflecting the electrochemical reactions occurring on MCMB. The second (red dotted line) and third (green solid line) cycles show reproducible peak potentials. The electrochemical reactions have been previously described.^{5,7,28} In order to aid in the discussion in Section 3.3, the stoichiometric coefficients of the reactants and products in the electrochemical equations given below have been normalized to reflect the predicted relative intensities in the dOp NMR spectrum for a fixed amount of graphite. The electrochemical half-reaction for the peak labelled A corresponds to the transition to stage 4 (LiC_{36}) from stage 8 (LiC_{72}), and is described by

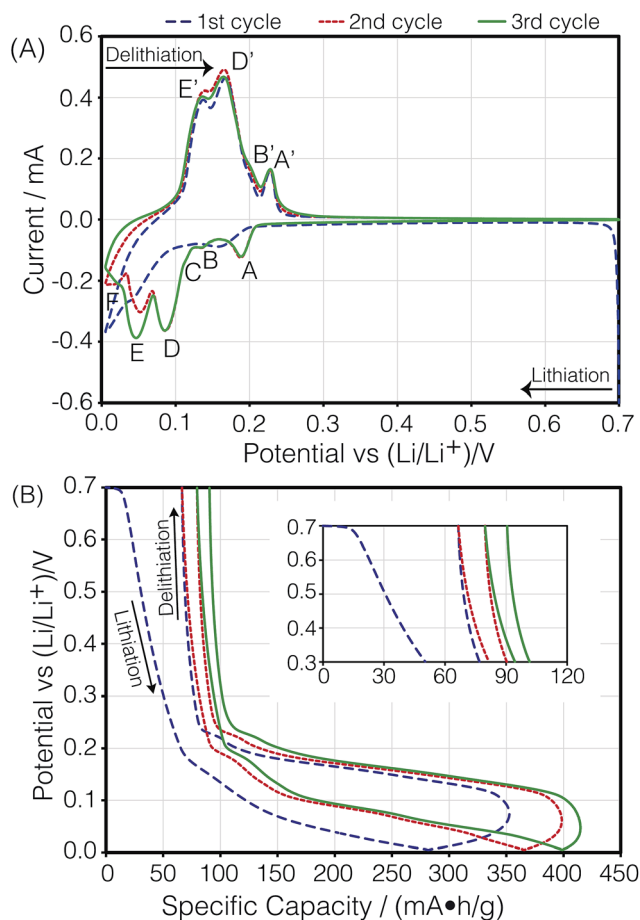
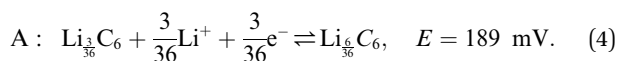
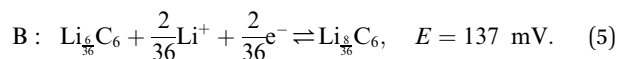


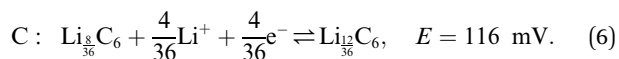
Fig. 3 (A) Cyclic voltammogram of the carbon/Li electrochemical cell depicting lithiation as a function of potential at $2 \mu\text{V s}^{-1}$. (B) Specific capacity during the cycling of the cell as a function of cell potential. The peaks labelled A, B, C, D, E, and F are described in the text.



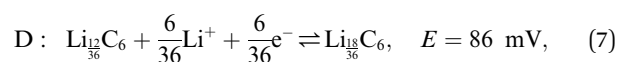
Similarly, the peak labelled B corresponds to the formation of stage 3 (LiC_{27}), and is described by



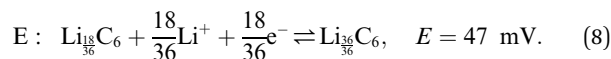
The shoulder labelled C at 116 mV suggests the transition to stage 2L (LiC_{18}), and is described by



The peak labelled D corresponds to the formation of stage 2 (LiC_{12}), and is described by



and finally the peak labelled E is the transition to stage 1 (LiC_6), and is described by



The transition to form stage 8 (LiC_{72}), also known as dilute stage 1, has no evident peak in the CV. Peak F at near 15 mV will be discussed later in the text.

Fig. 3B shows the cell's specific capacity as a function of cell potential. The plot was obtained by integrating the currents in the CVs as a function of potential and normalizing them to the sweep rate. Even though the first cycle achieved a specific capacity of 353 mA h g^{-1} during lithiation, which is higher than the reported value from the manufacturer of 345 mA h g^{-1} , the delithiation capacity for the cycle was $286.5 \text{ mA h g}^{-1}$, giving an irreversible capacity of 66.5 mA h g^{-1} . Specific capacities of 332 and 335 mA h g^{-1} were attained for the second and third lithiation of the cell, with smaller irreversible capacities of 13.2 and 10.8 mA h g^{-1} , respectively. This trend was expected as it has been previously shown that the SEI is primarily formed during the first cycle of the cell, but small amounts continue to form during the subsequent cycles.^{29,30}

3.2 Conventional NMR spectrum

Before discussing the dOp spectrum we first review the spectral features of the conventional operando ^7Li NMR spectrum as a function of operando time or cell potential. The operando ^7Li NMR spectrum for the second cycle is shown in Fig. 4. The operando ^7Li NMR spectrum for all three cycles is given in the ESI†. The corresponding potential at which lithiation and delithiation occur is shown on the left vertical axis of Fig. 4 along with the corresponding cyclic voltammogram. The sharp ^7Li NMR resonances due to the electrolyte and SEI resonances near $\delta = 0 \text{ ppm}$ remain relatively constant at all operando times.

The signal intensity at 274 ppm from lithium metal arises from sites inside a skin depth of $12.3 \mu\text{m}$ even though the lithium electrode thickness is 0.3 mm . As shown earlier^{16,21} with the growth of lithium dendrites during the delithiation process on each cycle there is a dramatic increase in signal intensity as the lithium dendrites can be fully penetrated by the radio frequency of the NMR. Due to the fact that no dendrites are present during lithiation on the first cycle, no changes in the metallic lithium signal intensity are observed (see Fig. S1 of ESI†). The noticeable drop in lithium metal signal intensity at $t_{\text{op}} = 280 \text{ h}$ ($E_{\text{op}} = 74 \text{ mV}$) corresponds to the complete removal of deposited lithium dendrites on the counter electrode during lithiation of the graphite. Conversely, the reappearance of lithium dendrite resonance during the delithiation of carbon in the 2nd cycle occurs at approximately $t_{\text{op}} = 310 \text{ h}$ ($E_{\text{op}} = 152 \text{ mV}$).

At the beginning of the second cycle—the bottom of Fig. 4—between $t_{\text{op}} = 193 \text{ h}$ ($E_{\text{op}} = 700 \text{ mV}$) and $t_{\text{op}} = 225 \text{ h}$ ($E_{\text{op}} = 470 \text{ mV}$), we observe a broad featureless resonance of low intensity spanning a range of negative (diamagnetic) shifts from $\delta = -70 \text{ ppm}$ to 0 ppm that progressively narrows while shifting towards 0 ppm during lithiation. On delithiation this peak reappears at $t_{\text{op}} = 365 \text{ h}$ ($E_{\text{op}} = 549 \text{ mV}$), broadening and moving to more negative (diamagnetic) shifts until the end of

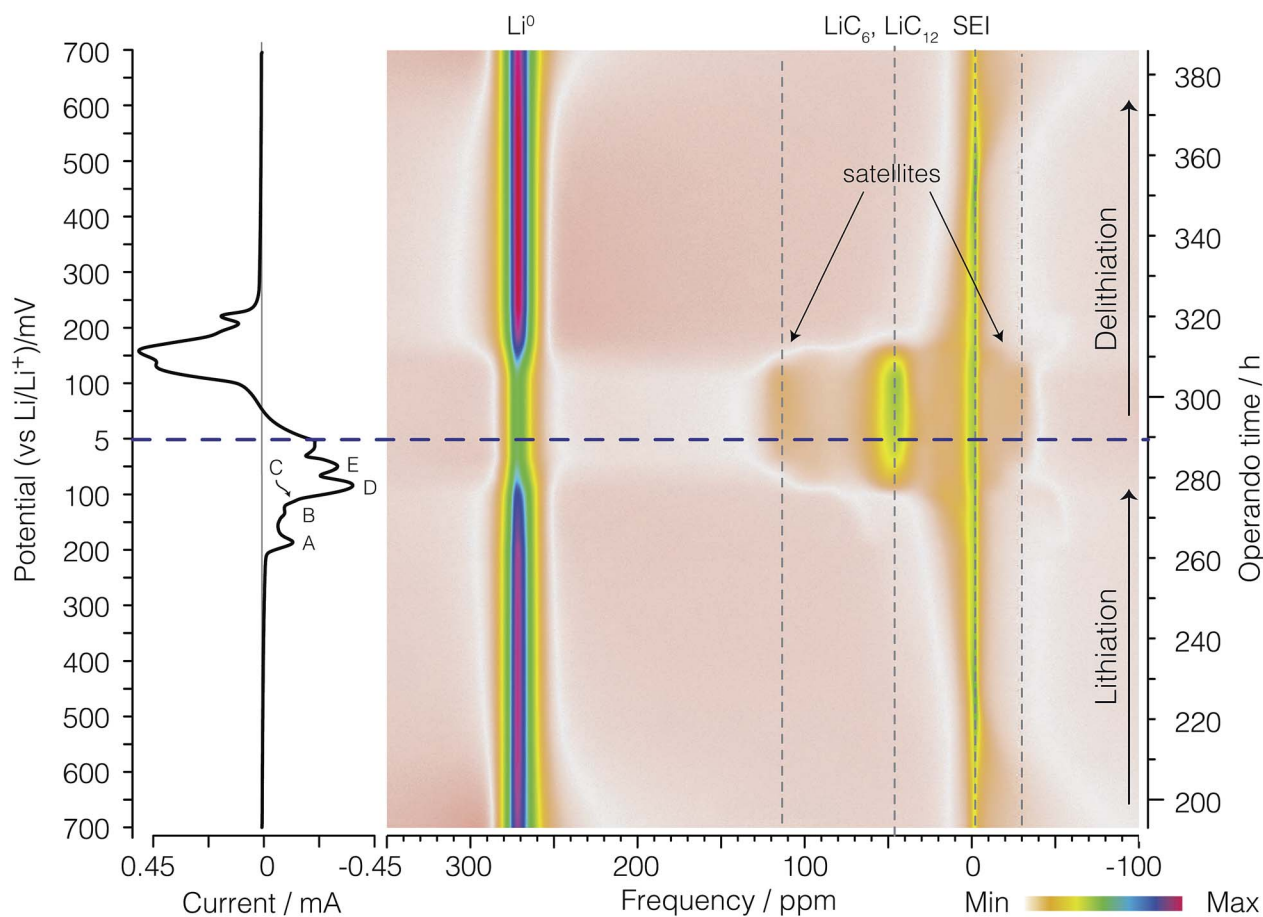


Fig. 4 A color intensity plot of the operando ^7Li NMR spectra of the second cycle of the electrochemical cell. Light colors represent low peak intensities and darker colors represent higher peak intensities. The horizontal axis shows the NMR frequency shift in ppm with reference to 1 M LiCl. The vertical axis shows the operando time for the second cycle of the cell. The horizontal blue (dashed) line represents the time at which the current polarity is switched. On the left is the corresponding cyclic voltammogram. Peaks labelled A, B, C, D, and E represent the formation of LiC_{36} , LiC_{27} , LiC_{18} , LiC_{12} , and LiC_6 respectively as shown in eqn (4), (5), (6), (7), and (8), respectively.

the cycle at $t_{\text{op}} = 386$ h ($E_{\text{op}} = 700$ mV). This broad resonance does not appear as mentioned in previous work. The assignment of this resonance is discussed in Section 3.3.

Between $t_{\text{op}} = 222$ h ($E_{\text{op}} = 490$ mV) and $t_{\text{op}} = 234$ h ($E_{\text{op}} = 400$ mV) a boost in the signal intensity around -2.5 ppm to -1 ppm is observed in a region also associated with the electrolyte and SEI resonances and appears with maximum intensity around $t_{\text{op}} = 226$ h ($E_{\text{op}} = 460$ mV). On delithiation this peak appears at $t_{\text{op}} = 341$ h ($E_{\text{op}} = 376$ mV) and lasts until $t_{\text{op}} = 361$ h ($E_{\text{op}} = 520$ mV). This resonance was tentatively assigned to the gas-like stage, LiC_{72} , by Chevallier *et al.*¹⁶ In contrast to this previous work,¹⁶ we observe no discernible quadrupolar satellite transition singularities in the line shape of this phase, although the sensitivity of our NMR spectrum may not be sufficient to observe these low lying intensities.

After the formation of LiC_{72} , between $t_{\text{op}} = 226$ h ($E_{\text{op}} = 460$ mV) and $t_{\text{op}} = 263$ h ($E_{\text{op}} = 196$ mV), the intercalated lithium resonances continue to move to more positive shifts while approximately doubling in line width from a fwhm of 10 ppm to 20 ppm. On delithiation these resonances appear at $t_{\text{op}} = 321$ h ($E_{\text{op}} = 232$ mV) and last until $t_{\text{op}} = 345$ h

($E_{\text{op}} = 405$ mV). As with the LiC_{72} we observe no discernible quadrupolar satellite transition singularities in the line shape of these resonances.

The ^7Li NMR resonance of the first dilute stage of lithiated graphite, LiC_{36} , begins appearing at $t_{\text{op}} = 263$ h ($E_{\text{op}} = 196$ mV) near $\delta = 1$ ppm with quadrupolar satellite transition singularities flanking at ± 9 kHz (± 58 ppm). The appearance of this resonance coincides with the appearance of peak A in the CV on the left of the spectrum. This intercalated lithium resonance continues to move to more positive shifts from 1 to about 6 ppm while maintaining the same quadrupolar splitting until the resonance becomes obscured by its disappearance and the growth of the overlapping resonance from LiC_{27} at $t_{\text{op}} = 271$ h ($E_{\text{op}} = 137$ mV) and 6 ppm with quadrupolar satellite transition singularities flanking at ± 9 kHz (± 58 ppm).

The dense stages 1 and 2 appear with the strongest intensity at $\delta = -50$ ppm to 120 ppm between $E_{\text{op}} = 74$ mV ($t_{\text{op}} = 280$ h) and $t_{\text{op}} = 310$ h ($E_{\text{op}} = 152$ mV). The resonances for the two ^7Li satellite transitions of stages 4 through 1 have characteristic quadrupolar powder pattern line shapes associated with $\eta_{\text{q}} \approx 0$. The two perpendicular powder pattern singularities are

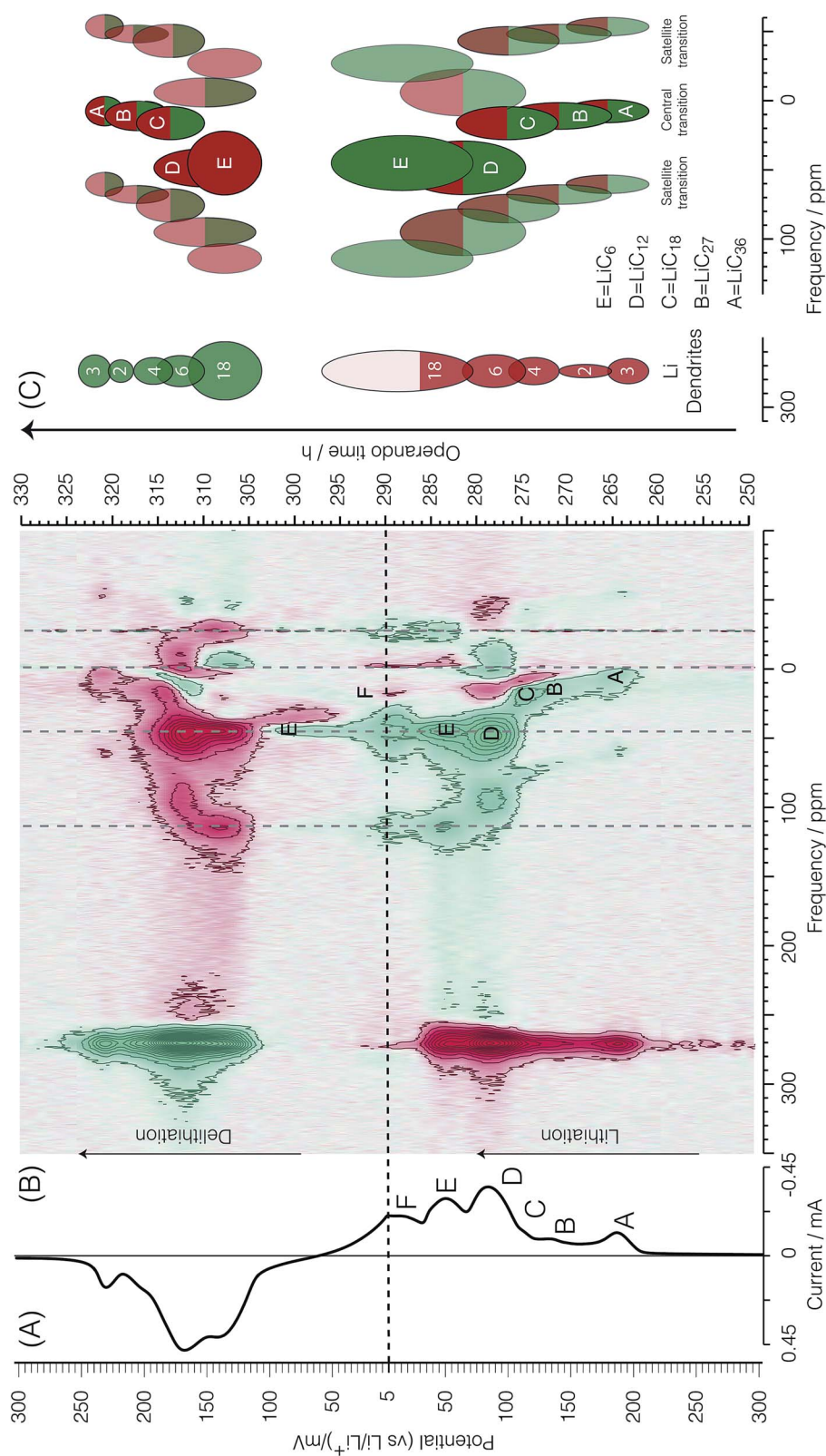


Fig. 5 (A) Cyclic voltammogram of the second cycle of the cell. (B) Corresponding bicolor dOp NMR spectrum as a function of time in the potential range between 300 and 5 mV. (C) Schematic representation of the lithiation and delithiation of a carbon electrode. The colored areas have been normalized to reflect the relative intensities in the NMR spectrum for a fixed amount of graphite and to match the stoichiometric coefficients of the reactants and products in the electrochemical equations.

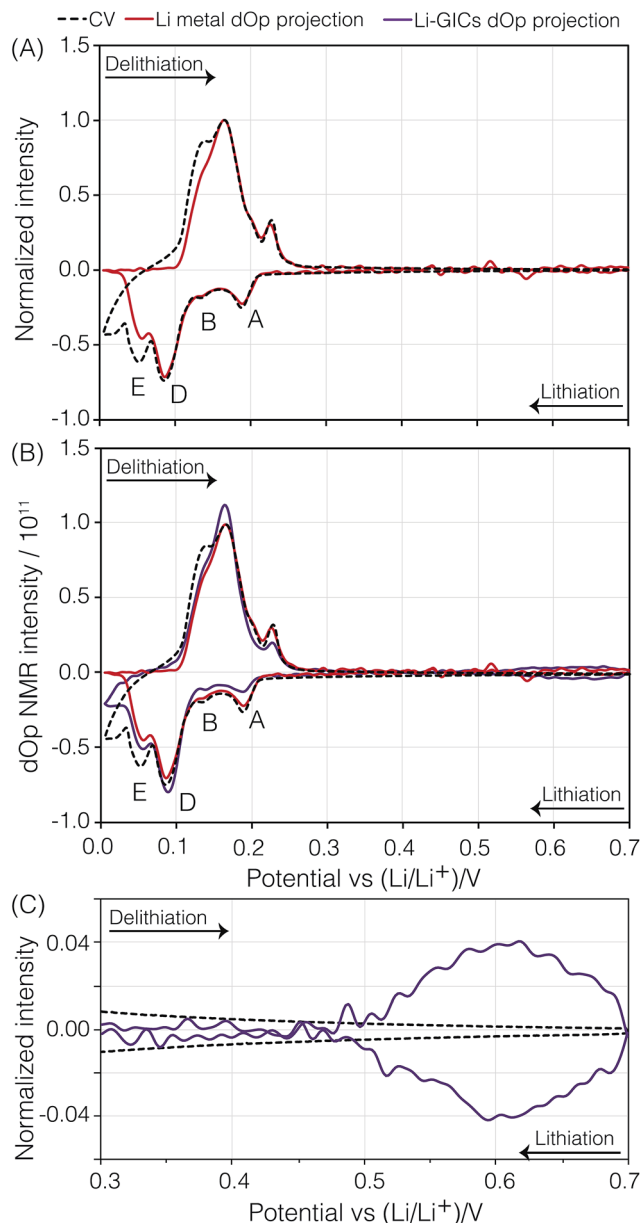


Fig. 6 (A) Electrochemical current CV (black dashed line) and the “dOp-NMR cyclic voltammogram” (red line) taken from the projection of the ⁷Li dOp-NMR signal across the lithium metal for the second cycle of the carbon/Li electrochemical cell. (B) Comparison of the dOp-NMR CV taken from the projection of the ⁷Li dOp-NMR signal across the lithium metal (red dashed line) and the projection of the Li-GICs (purple line) to the electrochemical CV. (C) Comparison of the dOp NMR CV and the electrochemical CV in the region between 700 and 300 mV depicting the formation of LiC₇₂ and precursors. The peaks labelled A, B, D, and E were previously described in the text.

observed at frequencies that flank the central transition at ± 8 kHz to ± 11 kHz depending on the site.

3.3 dOp NMR spectrum

Fig. 5 and 7 show the dOp ⁷Li NMR spectrum split into two parts for the late and early stages of lithiation, respectively. The dOp NMR spectrum is obtained by taking the first derivative of the

conventional two-dimensional NMR spectrum with respect to t_{op} as described in Section 2.2.2. Positive derivative intensities are shown in green and represent the formation of lithium species (henceforth called formation peaks) whereas negative derivative intensities are shown in red and represent the removal of lithium species (henceforth called removal peaks). As noted earlier the signal at 274 ppm arises from the lithium metal. In stark contrast to the conventional NMR spectrum in Fig. 4 we clearly see in the dOp NMR spectrum of Fig. 5 the high rate of removal of lithium metal during lithiation as the intense red resonance region from $t_{op} = 250$ h ($E_{op} = 300$ mV) to $t_{op} = 290$ h ($E_{op} = 5$ mV) and the strong rate of formation of lithium metal during delithiation as the intense green resonance region from $t_{op} = 290$ h ($E_{op} = 5$ mV) to $t_{op} = 326$ h ($E_{op} = 268$ mV). The intensity of the lithium signal (rate of dendrite removal) behaves in a manner completely analogous to a CV with the lithium metal NMR derivative intensity correlated with electrochemical current as shown in Fig. 6A (*vide infra*). Similarly, the ⁷Li dOp NMR resonances assigned to the formation and removal of the intercalated graphite stages are clearly visible as the green and red resonances in the region from -50 ppm to 150 ppm. As expected, the formation peaks of the GIC are correlated with the removal peaks of the lithium metal and *vice versa*. Compared to the conventional NMR spectrum, however, the dOp spectrum reveals considerably more details about the chemistry of the lithiation and delithiation processes as we describe in further detail below.

3.3.1 Li metal resonance. In the case of the lithium metal resonance it is important to remember, as noted earlier with the conventional NMR signal, that its intensity arises primarily from the dendritic structures. Thus the lithium metal dOp signal narrows dramatically at $t_{op} = 287$ h ($E_{op} = 23$ mV) and completely disappears from the spectrum at $t_{op} = 291$ h ($E_{op} = 16$ mV), indicating that the lithium electrode has run out of dendrites. At this point the cell continues to consume lithium from the skin of the metal electrode, but because of rf skin depth effects the conventional lithium metal NMR signal experiences no changes in intensity and thus vanishes from the dOp NMR spectrum. During delithiation the dOp signal of the lithium metal reappears as dendrites are formed at $t_{op} = 304$ h ($E_{op} = 105$ mV) and persists as dendrites continue to form until $t_{op} = 326$ h ($E_{op} = 268$ mV).

Presuming that the concentration of each lithium species in the cell is proportional to the NMR signal intensity in the conventional NMR spectrum, then the change in the NMR signal as a function of time is correlated with the electrochemical current measured at each operando time/potential. If we take the projection of the dOp spectra in the frequency range between 200 ppm and 350 ppm and plot it in a cyclic manner we obtain the “dOp-NMR Cyclic Voltammogram” shown in Fig. 6A. The reaction rates along the vertical axis of both the dOp-NMR CV and electrochemical current CV were normalized for better comparison. During lithiation of carbon, we see excellent agreement between the CV and the dOp-NMR CV of the lithium metal until about 50 mV where dendrites start to deplete and the dOp NMR signal dies. Similarly at the beginning of delithiation, mossy like structures grow on the surface of the

lithium metal electrode that do not get fully penetrated by the NMR radio frequency like dendrites, and result in a weaker signal in the dOp NMR spectrum than that observed in the CV. Overall, the dOp NMR spectrum shows a strong correlation with the electrochemical currents implying that for every electron transferred from the system, a lithium ion is removed from the counter electrode. The numbers in circles in the metal signal in the schematic on the right of Fig. 5 correspond to the numerator of the lithium ion fraction in the corresponding half-reaction. These numbers roughly correspond to the area of the dOp lithium metal resonance in the region correlated with each half-reaction.

3.3.2 Lithiation of dilute stages. Next we shift our focus to the dilute stages, LiC_{36} , LiC_{27} , and LiC_{18} , whose formation appears in the dOp NMR spectrum between $t_{\text{op}} = 264$ h ($E_{\text{op}} = 189$ mV) and $t_{\text{op}} = 275$ h ($E_{\text{op}} = 112$ mV) and are labelled A, B, and C, respectively, and the removal appears in the dOp NMR spectrum between $t_{\text{op}} = 310$ h ($E_{\text{op}} = 153$ mV) and $t_{\text{op}} = 323$ h ($E_{\text{op}} = 246$ mV) in Fig. 5. On the right of Fig. 5 we also include a schematic diagram to illustrate the overlap of formation and removal peaks to aid in the discussion that follows.

LiC_{36} . Fig. 5 clearly shows a formation peak labelled A around $\delta = 4$ ppm at $t_{\text{op}} = 264$ h ($E_{\text{op}} = 189$ mV). This peak correlates with the cathodic peak labelled A in the electrochemical voltammogram and is assigned to the formation of LiC_{36} which is described by eqn (4). Formation peak A is also more clearly seen in the dOp NMR spectrum to be flanked on both sides by two peaks appearing at $\delta \approx 4 \pm 60$ ppm due to the satellite transitions of ^7Li , a spin $I = 3/2$ nucleus. Associated with this formation peak is a corresponding removal peak (red) at $\delta = 274$ ppm from lithium dendrite removal. Removal of the previous phase LiC_{72} is also observed by a faint removal peak at 0 ppm. In the schematic diagram on the right of Fig. 5 we indicate the LiC_{36} (green) formation peak with a green central transition line and its two satellites along with a corresponding lithium dendrite (red) removal peak. In the schematic on the right of Fig. 5 the satellite areas are made transparent to match their lower peak intensity compared to the central transition line. This process of formation of LiC_{36} will be further discussed in Section 3.3.5.

LiC_{27} . The formation peak labelled B at $\delta \approx 10$ ppm and $t_{\text{op}} = 270$ – 272 h ($E_{\text{op}} = 150$ – 137 mV) in the dOp NMR spectrum in Fig. 5 correlates with the formation of the cathodic peak labelled B in the electrochemical voltammogram. This peak is assigned to the formation of LiC_{27} associated with the half-reaction of eqn (5). This formation peak is also flanked on both sides by two formation peaks appearing at $\delta \approx 10 \pm 60$ ppm due to the satellite transitions. Homologous removal peaks for LiC_{36} at 10 ppm and lithium dendrites at $\delta = 274$ ppm are also observed. Note that the corresponding removal peak of lithium dendrite drops in intensity compared to the previous reaction, which is consistent with the reduction of the stoichiometric coefficient of Li^+ by 1/3 from the half reaction A to B.

LiC_{18} . The strong formation peak labelled C at 15 ppm and $t_{\text{op}} = 274$ h ($E_{\text{op}} = 117$ mV) in the dOp NMR spectrum correlates with the formation of the cathodic peak labelled C in the electrochemical voltammogram. As previously mentioned, the electrochemical voltammogram shows LiC_{18} as a shoulder

(peak C) during the formation of LiC_{12} . Therefore, this dOp peak is assigned to the formation of LiC_{18} as part of the half-reaction of eqn (6). Associated with this half-reaction is the removal peak of LiC_{27} at $\delta \approx 10$ ppm for its central transition. Again, the power of the dOp approach is apparent considering that the transition from LiC_{36} to LiC_{18} is not discernible in the conventional NMR spectrum in Section 3.2. The higher intensity of the removal peak for LiC_{27} in the dOp spectrum is due to the higher lithium concentration of the phase compared to the former phases. LiC_{18} also shows two satellite transition peaks appearing at $\delta \approx 15 \pm 60$ ppm. During its formation the lithium dendrite removal peak does not show a well-defined area due to the low electrochemical resolution between this phase and the next (LiC_{12}).

3.3.3 Lithiation of dense stages

LiC_{12} . Fig. 5 also shows the dOp NMR spectrum of the dense stages of lithiation LiC_{12} and LiC_6 . These phases are seen in the conventional NMR spectrum (Section 3.2) by a broad, strong signal at $\delta \approx 45$ ppm with two perpendicular powder pattern singularities at frequencies that flank the central transition at ± 8 to ± 11 kHz depending on the site. The dOp spectrum, in contrast, shows well resolved areas for both phases. Accumulation of LiC_{12} is visible as a strong formation peak at $t_{\text{op}} = 275$ h ($E_{\text{op}} = 112$ mV) at $\delta \approx 48.3 \pm 48$ ppm, and as seen in eqn (7), results from further lithiation of graphite as lithium metal and LiC_{18} are removed. The LiC_{18} removal peaks for the central and one of the satellite transitions occur at 15 ppm and -50 ppm, respectively. The dOp intensity of lithium dendrites decreased (intense red) drastically due to the faster rates of removal of lithium to form LiC_{12} . This transition is depicted in the CV by a broad reduction peak at $E_{\text{op}} = 85$ mV labelled D. Due to the higher NMR shift and similar quadrupolar frequencies of this phase compared to those of the dilute stages, it is easier to discern the formation of the LiC_{12} central transition and both satellites as the previous LiC_{18} phase (peak C) is removed. This behavior is illustrated in the schematic diagram on the right of Fig. 5, where the satellite at $\delta \approx 0$ ppm from LiC_{12} (peak D) grows at an NMR shift that is between the central and right satellite removal peaks of C.

LiC_6 . As lithiation continues LiC_6 is formed according to eqn (8) and peak E appears at $\delta \approx 42$ ppm and $t_{\text{op}} = 281$ h ($E_{\text{op}} = 66$ mV) in the dOp spectrum. Due to the close proximity of the central transitions of LiC_6 and LiC_{12} there is strong overlap of their corresponding formation and removal peaks, respectively, making the central transition of the LiC_6 in the dOp spectrum appear narrower and lower in intensity than expected based on the stoichiometry. The strong growth of LiC_6 is, however, observed in the dOp spectrum at both its flanking satellite transition formation peaks at 110 ppm and -26 ppm while a red peak at 0 ppm confirms the removal of the right satellite LiC_{12} . The formation of LiC_6 is observed until $t_{\text{op}} = 296$ h ($E_{\text{op}} = 51$ mV). In this potential range thermodynamics still favors the Li reduction even though the cell is being swept in the opposite (oxidation) direction as the potential is not sufficiently positive to oxidize (or delithiate) Li from the carbon structure due to the irreversible nature of the chemical reaction. In other words, at potentials where Li insertion is

favorable, and if the underlying carbon is not fully lithiated to 100%, Li will continue to move into the carbon structure and form LiC_6 at these potentials regardless of the direction of the potential sweep. Since the lithium electrode has run out of dendrites at this stage an expected lithium metal removal peak at $\delta = 274$ ppm correlated with LiC_6 formation is not observed.

Lithium naphthalenide. At the end of lithiation a cathodic peak at $t_{\text{op}} = 288.5$ h ($E_{\text{op}} = 15$ mV), labelled F, is noted in the CV. It has been previously reported that at these negative potentials Li-Li clusters contained in the structure LiC_2 can be formed as well as the formation of lithium naphthalenide by the bonding of lithium atoms to the edging carbons of the graphene sheets in MCMB.^{31,32} The formation of Li-Li clusters is characterized by an NMR shift close to that of metallic lithium due to the strong metallic character of the Li-Li bond. Our experiments do not reveal such an NMR shift and therefore, we can

infer that the cathodic peak in the CV may be related to the formation of the ionic complex lithium naphthalenide. This compound has no discernible quadrupolar satellite transition singularities in the line shape and has been previously explained by Chevallier *et al.*¹⁶ to form as the formation of LiC_{12} starts. Although there is an NMR signature for lithium naphthalenide present in the conventional NMR spectrum, there is no clear evidence of such a signature in the dOp spectrum due to the overlapping NMR shift for the delithiation of LiC_{18} . The formation of this compound can be inferred by the smaller removal peak width of the LiC_{12} satellite at 0 ppm, contrary to what has been illustrated in the schematic of Fig. 5.

3.3.4 Delithiation of dense and dilute stages. The dOp NMR spectrum in Fig. 5 also shows the delithiation process of the dense to dilute stages of carbon lithiation with more details compared to the conventional NMR spectrum. At $t_{\text{op}} = 290$ h

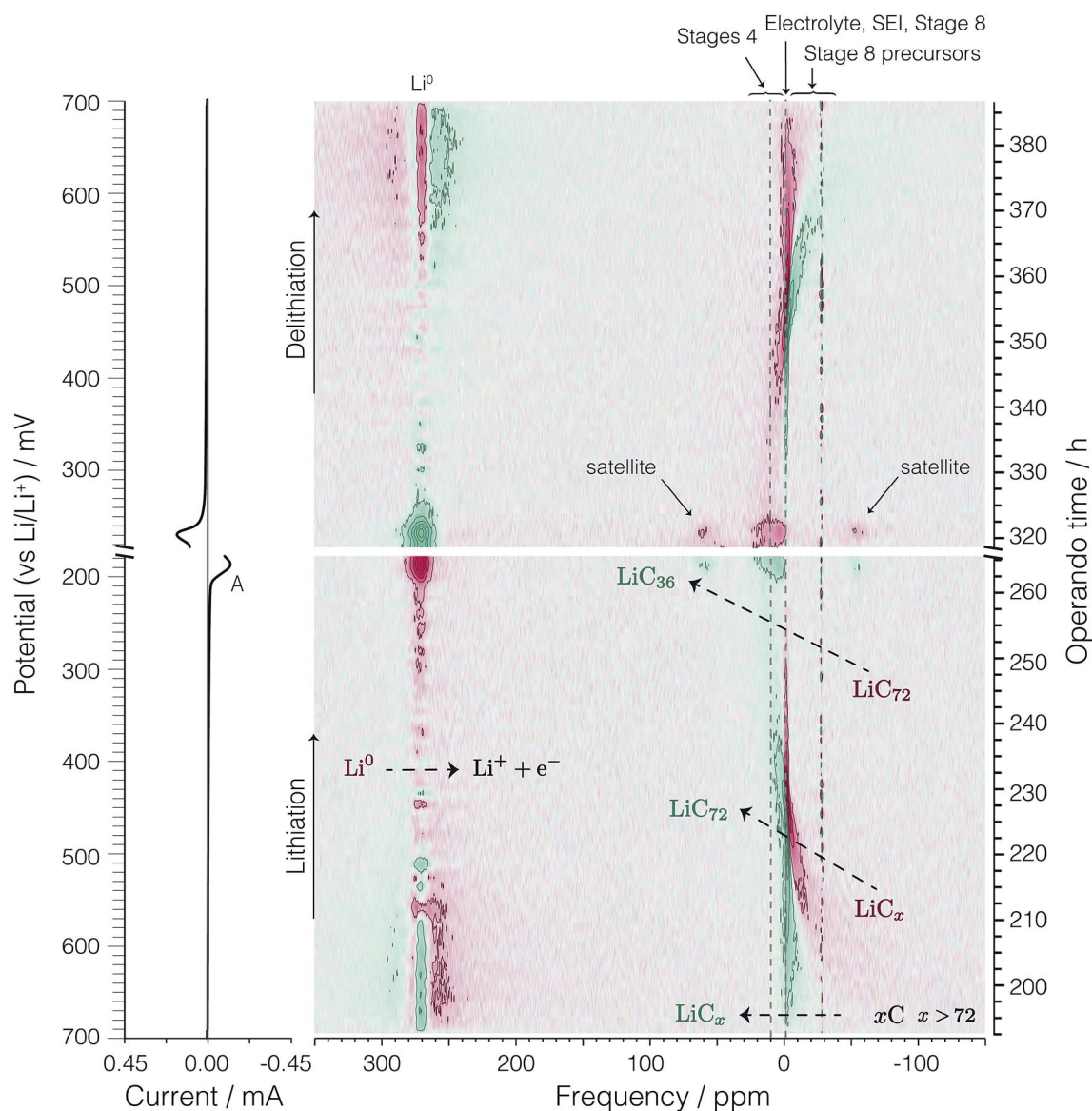


Fig. 7 On the left is the cyclic voltammogram of the second cycle of the cell and on the right is the corresponding bicolor dOp NMR spectrum as a function of time in the potential range between 700 and 200 mV during lithiation and delithiation.

($E_{\text{op}} = 5$ mV) the current polarity is reversed and delithiation begins. From $t_{\text{op}} = 295$ h ($E_{\text{op}} = 45$ mV) to $t_{\text{op}} = 303$ h ($E_{\text{op}} = 102$ mV) the signal from LiC_6 is seen to have a mixture of both positive and negative intensities due to a change in the phasing of the spectrum, however, the net dOp NMR signal averages to zero in this time/NMR shift range. At $t_{\text{op}} = 303$ h ($E_{\text{op}} = 102$ mV) intense removal peaks are observed at $\delta \approx 45 \pm 70$ ppm indicating the delithiation of LiC_6 while a green peak appears at approximately -10 ppm for the formation of the right satellite LiC_{12} . Similarly, a strong formation peak is observed at 274 ppm for the deposition of lithium dendrites.

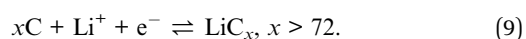
Further delithiation results in a formation peak at approximately 15 ppm at $t_{\text{op}} = 310$ h ($E_{\text{op}} = 152$ mV) for the evolution of the LiC_{18} central transition as well as at 274 ppm for the deposition of more dendritic lithium. It is important to note that on delithiation, the peaks for LiC_{27} and LiC_{18} cannot be distinguished in the dOp spectrum due to the fast rates of delithiation of the carbon electrode. However, our potential window experiments have shown that the oxidation peak that appears as a shoulder during the delithiation of LiC_{12} in the CV at $t_{\text{op}} = 317$ h ($E_{\text{op}} = 205$ mV) corresponds to the delithiation of LiC_{27} and the oxidation peak for the delithiation of LiC_{18} is buried underneath the removal peak of LiC_{12} .

The removal peak around $\delta = 4$ ppm for LiC_{36} during delithiation appears at $t_{\text{op}} = 321$ h ($E_{\text{op}} = 232$ mV), while formation peaks are observed at 274 and 0 ppm representative of dendrite and LiC_{72} formation, respectively. This transition is correlated with the oxidation peak seen in the electrochemical voltammogram at 230 mV.

3.3.5 Lithiation of gas-like stages

Precursors to LiC_{72} . Fig. 7 shows the dOp spectrum of the lithiation processes occurring at potentials between 700 and ~ 200 mV—where the formation of LiC_{36} occurs—and the delithiation processes occurring between ~ 200 mV and the end of the cycle at 700 mV.

At the beginning of the cycle at $t_{\text{op}} = 193$ h ($E_{\text{op}} = 700$ mV) and up to about $t_{\text{op}} = 230$ h ($E_{\text{op}} = 430$ mV) the conventional NMR spectrum in Fig. 4 shows a broad area of negative shifts that continuously narrows while shifting more positively. The dOp NMR spectrum in Fig. 7, in contrast, shows the appearance of a sharp formation peak with shifts between 0 and -15 ppm while broad, low intensity red peaks with negative (diamagnetic) shifts disappear. These negatively shifted peaks are observed to progressively narrow while shifting towards 0 ppm during lithiation, indicating the formation of GICs in stages higher than 8, which we call “precursors” for simplicity.



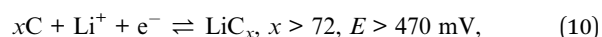
The broad NMR line shape of these precursors indicates a distribution of NMR signals arising from the different lithium environments that conform to the precursors.

Theoretical and computational calculations^{33–35} have shown that the band structure of graphite changes from a narrow band semiconductor to a conductor when lithium ions intercalate into the graphene sheets due to the injection of electrons from the external circuit that are delocalized within the graphene

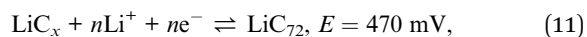
layers. The magnetization of free conduction electrons on these layers results in an enhancement of the magnetic field experienced by the lithium nuclei, explaining the ^7Li NMR Knight shifts observed for the GICs with stages lower than 4.³⁶ The diamagnetic shifts observed for the Li–GIC precursors suggest that at this stage during lithiation not enough electrons have been injected into the graphene layers to make them conducting and therefore, no Knight shifts are observed in the ^7Li NMR of the Li–GIC precursors.

LiC_{72} . Between $t_{\text{op}} = 215$ h ($E_{\text{op}} = 542$ mV) and $t_{\text{op}} = 234$ h ($E_{\text{op}} = 400$ mV) the intensity of a formation peak at around -2.5 to -1 ppm, tentatively assigned to LiC_{72} by Chevallier *et al.*,¹⁶ intensifies while the broad diamagnetic removal peaks narrow and shift to more positive values. This formation peak is observed to reach maximum intensity at $t_{\text{op}} = 225$ h ($E_{\text{op}} = 470$ mV). No discernible quadrupolar satellite transition singularities are observed in the line shape of this formation peak. Assuming that the total lithium transferred to the system up to this potential ($E_{\text{op}} = 470$ mV) is used to form Li–GICs then the total charge and moles of lithium calculated result in a Li–C stoichiometry of LiC_{69} , which is close to that of stage 8 LiC_{72} . Thus, we confirm the assignment of this unknown formation peak to LiC_{72} .

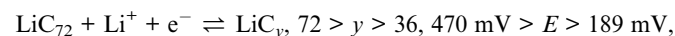
Pre-dilute stages. After the formation of LiC_{72} at $t_{\text{op}} = 225$ h ($E_{\text{op}} = 470$ mV) its corresponding formation peak continues to move towards more positive shifts as it broadens and disappears from $t_{\text{op}} = 237$ h ($E_{\text{op}} = 383$ mV) to $t_{\text{op}} = 260$ h ($E_{\text{op}} = 218$ mV). Similarly, the loss of LiC_{72} is seen by the red removal peak at around 0 ppm from $t_{\text{op}} = 225$ h ($E_{\text{op}} = 470$ mV) to $t_{\text{op}} = 260$ h ($E_{\text{op}} = 218$ mV) where the formation peak of LiC_{36} becomes visible. The broadening in the line shape might be due to a continuous lithium packing into the graphene layers, resulting in broad, low intensity NMR peaks that continuously shift from 1 ppm to 6.3 ppm from the distribution of phases occurring during this transition. No discernible quadrupolar satellite transition singularities are observed in the line shape of these phases. On the basis of these results we write the electrochemical half-reactions during lithiation of the GICs for the precursors as



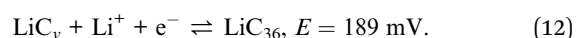
followed by the formation of LiC_{72} as



and proceeding up to stage 4 as



and



3.3.6 Delithiation of gas-like stages. The upper section of Fig. 7 shows the dOp NMR spectrum of the delithiation process from LiC_{36} to the end of the cycle. The first evidence of the delithiation of LiC_{36} occurs at $t_{\text{op}} = 341$ h ($E_{\text{op}} = 376$ mV), where

a green signal at $\delta \approx 0$ ppm and a faint red signal at $\delta \approx 10$ ppm are observed. This transformation lasts until $t_{\text{op}} = 361$ h ($E_{\text{op}} = 520$ mV), where the formation of the precursors is then observed as LiC_{72} is removed, indicating that both of these transitions are reversible processes.

3.3.7 dOp NMR vs. electrochemical CVs. As described in Section 3.3.1, we similarly take the projection over the GIC resonances of the dOp spectra in the frequency range between 160 to -200 ppm and plot it in a cyclic fashion to obtain the “dOp-NMR Cyclic Voltammogram”. Fig. 6B shows the overlay of the dOp NMR CV of the GICs and lithium metal, and the electrochemical CV. The electrochemical current was normalized and the negative derivative, due to the formation of lithiated GIC species from the dOp NMR projection, was assigned to the cathodic currents. A direct correlation of the peak potentials suggests that there is no delay in the NMR response to the current perturbation at the sweep rate measured. Fig. 6C shows the overlay of the dOp NMR CV of the GICs and the electrochemical CV in the region between 700 and 300 mV. The electrochemical CV shows an increasing capacitance due to changes in the dielectric of the carbon as lithium is intercalated into the bulk, however, the dOp NMR CV of the GICs clearly shows the formation and removal of the precursors and LiC_{72} .

Although the dOp NMR CV of the GICs shows similar behavior for both the electrochemical current CV and the lithium metal dOp NMR CV, there are minor discrepancies among the relative intensities of the GIC CV peaks A, B, C, D, and E. The lower relative intensity of the GIC CV peaks A and B compared to the corresponding electrochemical current CV and the lithium metal dOp NMR CV peaks arises from the longer GIC relaxation times of A and B, and the subsequent lower fraction of transverse magnetization excited, as noted in Table 1. On the other hand, the GIC CV peak for D, with its shorter relaxation time, is reasonably close to the corresponding electrochemical current CV and the lithium metal dOp NMR CV peaks for D. Based on stoichiometry one would expect a lower intensity for D in all CVs. The apparent boost in D intensity is attributed to broader CV peaks of C and E which extend under the CV peak of D. This is more clearly visible in the 2D dOp NMR spectrum in Fig. 5 which shows that LiC_{12} (peak D) begins forming at $t_{\text{op}} = 275$ h ($E_{\text{op}} = 112$ mV), where the previous phase LiC_{18} (peak C) is still forming. Additionally, the formation of LiC_6 (peak E) is seen to begin at $t_{\text{op}} = 281$ h ($E_{\text{op}} = 66$ mV) while LiC_{12} is still being formed. Both of these overlapping formations result in a higher CV intensity for D due to possible inhomogeneity of the cell voltage within the electrode.

A direct comparison of the relative intensities or areas of the dOp NMR CV of the lithium metal to the GICs in Fig. 6B is complicated by a number of factors. The first is that the central transition equilibrium magnetization of the lithium metal is a factor of $S + 1/2 = 2$ times smaller than the full nuclear magnetization of the lithium in the GIC. The second is that the excitation pulse length used in these experiments corresponds to a 26° rotation of the central transition magnetization of the lithium metal and a 13° rotation of the full nuclear magnetization of the lithium in the GIC—giving approximately a factor of two better excitation efficiency for the lithium metal. Finally, the

significantly shorter T_1 of lithium metal leads to it having an ~ 3 times greater fraction of steady-state transverse magnetization than the GICs. The first two factors effectively cancel each other and the last factor, predicting the lithium metal signal area to be ~ 3 times greater than the GIC signal areas, is not what is observed. The most likely explanation is that two thirds of the expected lithium metal dOp signal is not observed due to skin depth effects.

Finally, we note that unrelated but another potential source of intensity error in the NMR can arise from drifts in the receiver phase during the operando experiment. Possible remedies for this source of error could include (1) auto tuning the probe during the acquisition,³⁷ (2) employing post-acquisition auto-phasing the spectra, or (3) in the case of spin $I \leq 3/2$, like ^7Li , the use of a total echo experiment³⁸ to eliminate dead time issues.

4 Conclusions

Although operando ^7Li NMR is a powerful technique for probing the changes that occur in the carbon electrode as it gets intercalated and deintercalated with lithium, the spectra often suffer from poor resolution due to a number of overlapping resonances. We have shown that a simple signal processing method of analyzing the operando NMR signal by taking the derivative of the signal with respect to the operando time, referred to as dOp NMR (derivative operando NMR), results in significantly more detailed information about the changes that occur during the cycling of the cell. By using this method we have identified the formation and removal of six stages of lithium intercalation and deintercalation from LiC_{72} to LiC_6 and back. In addition, the dOp NMR method allows for the detection of additional gas like stages of Li in graphite, which were previously not observed experimentally. In this work, using slow rates of potential perturbation at $2 \mu\text{V s}^{-1}$, we have identified the electrochemical potentials at which LiC_{72} is formed from gas like Li precursors.

A partial projection over specific regions of the dOp NMR spectrum as a function of the operando time or voltage can be presented in a cyclic fashion what is termed a dOp NMR CV. Through the dOp NMR CV method we have found that the rates of formation and removal of lithium dendrites ^7Li resonances closely follow the electrochemical current as long as dendrites are present in the cell. Similarly, the rates of formation and removal of ^7Li resonances associated with the lithium intercalated graphite also follow the electrochemical current flow with slight deviations due to an experimental artifact from incomplete ^7Li relaxation of Li stages as well as possible inhomogeneity of the cell voltage within the electrode in the electrochemical reactions after stage 3.

The dOp methodology could be applied to other operando analyses such as *in situ* XRD or *in situ* IR or Raman spectroscopy, where time independent processes can be removed to enhance the signals of relevant time dependent chemical transitions.

Conflicts of interest

There are no conflicts to declare.

Acknowledgements

This material is based upon work supported in part by the National Science Foundation under Seed Grant NSF-DMR-1420451. JLLL acknowledges the support of the GAANN fellowship from the Department of Education (P200A150267) and the Ohio State Department of Chemistry and Biochemistry.

References

- 1 T. Christen and M. W. Carlen, *J. Power Sources*, 2000, **91**, 210–216.
- 2 J.-M. Tarascon and M. Armand, *Nature*, 2001, **414**, 359–367.
- 3 B. Scrosati, J. Hassoun and Y.-K. Sun, *Energy Environ. Sci.*, 2011, **4**, 3287–3295.
- 4 B. Y. Liaw and R. Kostecki, *Electrochem. Soc. Interface*, 2011, **20**, 41–42.
- 5 J. R. Dahn, *Phys. Rev. B: Condens. Matter Mater. Phys.*, 1991, **44**, 9170–9177.
- 6 J. N. Reimers and J. R. Dahn, *J. Electrochem. Soc.*, 1992, **139**, 2091–2097.
- 7 T. Ohzuku, *J. Electrochem. Soc.*, 1993, **140**, 2490.
- 8 L. Y. Beaulieu, S. D. Beattie, T. D. Hatchard and J. R. Dahn, *J. Electrochem. Soc.*, 2003, **150**, A419.
- 9 S. Whitney, S. R. Biegalski, Y. H. Huang and J. B. Goodenough, *J. Electrochem. Soc.*, 2009, **156**, A886.
- 10 R. Downing, G. Lamaze, J. Langland and S. Hwang, *J. Res. Natl. Inst. Stand. Technol.*, 1993, **98**, 109.
- 11 D. X. Liu, L. R. Cao and A. C. Co, *Chem. Mater.*, 2016, **28**, 556–563.
- 12 D. X. Liu and A. C. Co, *J. Am. Chem. Soc.*, 2016, **138**, 231–238.
- 13 D. X. Liu, J. Wang, K. Pan, J. Qiu, M. Canova, L. R. Cao and A. C. Co, *Angew. Chem., Int. Ed.*, 2014, **53**, 9498–9502.
- 14 R. E. Gerald, J. Sanchez, C. S. Johnson, R. J. Klingler and J. W. Rathke, *J. Phys.: Condens. Matter*, 2001, **13**, 8269–8285.
- 15 M. Letellier, F. Chevallier and F. Béguin, *J. Phys. Chem. Solids*, 2006, **67**, 1228–1232.
- 16 F. Chevallier, F. Poli, B. Montigny and M. Letellier, *Carbon*, 2013, **61**, 140–153.
- 17 R. Bhattacharyya, B. Key, H. Chen, A. S. Best, A. F. Hollenkamp and C. P. Grey, *Nat. Mater.*, 2010, **9**, 504–510.
- 18 S. A. Krachkovskiy, J. D. Bazak, P. Werhun, B. J. Balcom, I. C. Halalay and G. R. Goward, *J. Am. Chem. Soc.*, 2016, **138**, 7992–7999.
- 19 H. J. Chang, A. J. Ilott, N. M. Trease, M. Mohammadi, A. Jerschow and C. P. Grey, *J. Am. Chem. Soc.*, 2015, **137**, 15209–15216.
- 20 J.-M. Tarascon, A. Gozdz, C. Schmutz, F. Shokoohi and P. Warren, *Solid State Ionics*, 1996, **86–88**, 49–54.
- 21 M. Letellier, F. Chevallier and M. Morcrette, *Carbon*, 2007, **45**, 1025–1034.
- 22 J. L. Markley, W. J. Horsley and M. P. Klein, *J. Chem. Phys.*, 1971, **55**, 3604–3605.
- 23 P. J. Grandinetti, J. T. Ash and N. M. Trease, *Prog. Nucl. Magn. Reson. Spectrosc.*, 2011, **59**, 121–196.
- 24 C. P. Slichter, *Principles of Magnetic Resonance*, Springer-Verlag, Berlin, 1980.
- 25 A. J. Ilott, S. Chandrashekar, A. Klöckner, H. J. Chang, N. M. Trease, C. P. Grey, L. Greengard and A. Jerschow, *J. Magn. Reson.*, 2014, **245**, 143–149.
- 26 R. R. Ernst, *Rev. Sci. Instrum.*, 1966, **37**, 93.
- 27 *RMN 1.1*, PhySy Ltd., 2017.
- 28 M. D. Levi and D. Aurbach, *J. Electroanal. Chem.*, 1997, **421**, 79–88.
- 29 A. J. Smith, J. C. Burns, X. Zhao, D. Xiong and J. R. Dahn, *J. Electrochem. Soc.*, 2011, **158**, A447.
- 30 M. A. McArthur, S. Trussler and J. R. Dahn, *J. Electrochem. Soc.*, 2012, **159**, A198–A207.
- 31 M. Hara, A. Satoh, N. Takami and T. Ohsaki, *J. Phys. Chem.*, 1995, **99**, 16338–16343.
- 32 K. Tatsumi, *J. Electrochem. Soc.*, 1996, **143**, 1923.
- 33 N. M. Caffrey, L. I. Johansson, C. Xia, R. Armiento, I. A. Abrikosov and C. Jacobi, *Phys. Rev. B*, 2016, **93**, 195421.
- 34 J.-C. Charlier, X. Gonze and J.-P. Michenaud, *Europhys. Lett.*, 1994, **28**, 403–408.
- 35 K. R. Kganyago and P. E. Ngoepe, *Phys. Rev. B: Condens. Matter Mater. Phys.*, 2003, **68**, 205111.
- 36 G. Volpillac and J. Hoarau, *Synth. Met.*, 1981, **4**, 77–79.
- 37 O. Pecher, D. M. Halat, J. Lee, Z. Liu, K. J. Griffith, M. Braun and C. P. Grey, *J. Magn. Reson.*, 2017, **275**, 127–136.
- 38 B. J. Walder, K. K. Dey, M. C. Davis, J. H. Baltisberger and P. J. Grandinetti, *J. Chem. Phys.*, 2015, **142**, 014201.

Supplement: Enhancing the Real-Time Detection of Phase Changes in Lithium-Graphite Intercalated Compounds Through Derivative Operando (dOp) NMR Cyclic Voltammetry

Jose L. Lorie Lopez¹, Philip J. Grandinetti^{1,*}, and Anne C. Co^{1,*}

¹Department of Chemistry and Biochemistry, The Ohio State University

^{*}Corresponding authors

November 6, 2017

S1 Calculation of lithium concentration and Li-C stoichiometry

From Figure 6 in the main text, the maximum intensity of the peak near 0 ppm was observed at $E_{\text{op}} \approx 477$ mV for the second and third cycles of the cell. The first cycle was not used to shift the peak potentials due to the pasivation of the electrodes. From Figure 3B, the integrated charge transferred to the system up to this potential was calculated to be $Q_{\text{op}} \approx 0.351$ C and $Q_{\text{op}} \approx 0.343$ C for the second cycle and third cycle, respectively.

The amount of lithium ions being transferred were calculated using the following equation:

$$[\text{Li}^+] = \frac{Q}{F}, \quad (1)$$

where Q is the charge in Coulombs and F is Faraday's constant. The resulting lithium ion concentration resulted in $[\text{Li}^+] = 3.637858 \times 10^{-6}$ mol and $[\text{Li}^+] = 3.554945 \times 10^{-6}$ mol for the second and third cycles respectively. Knowing that the amount of carbon in the electrode was 18.06 mg, the corresponding moles of C_6 was $[\text{C}_6] = 1.80338 \times 10^{-6}$ mol. The ratios of Li^+ to C_6 were then calculated to be 1:68 and 1:71 respectively, which average to 1:69 or a Li-C stoichiometry of LiC_{69} .

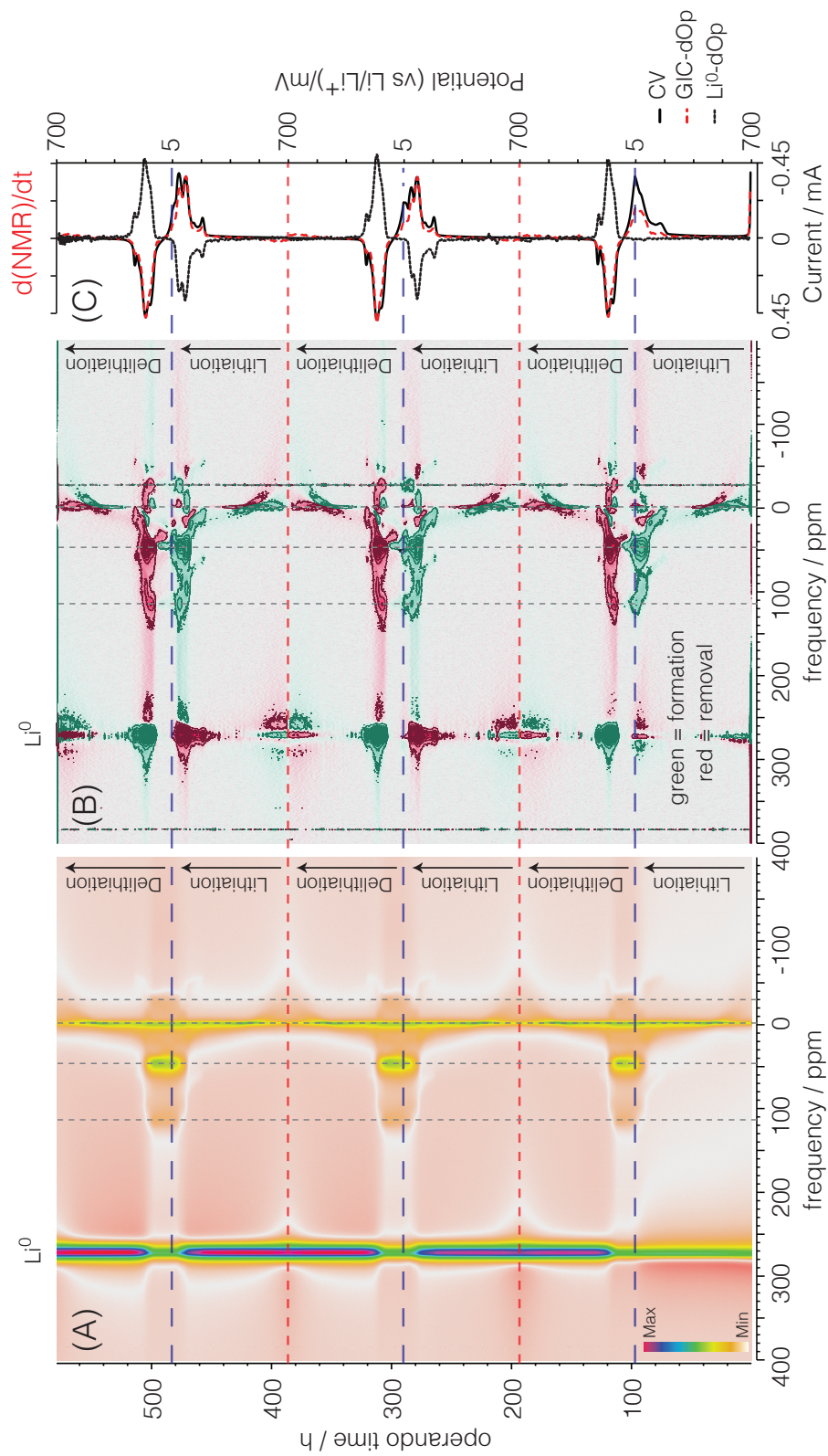


Figure S1: A) Color intensity plot of the operando ^7Li NMR spectra of all three cycles of the electrochemical cell. Light colors represent low peak intensities and darker colors represent higher peak intensities. The horizontal axis is the NMR frequency shift in ppm are referenced to 1 M LiCl. The vertical axis is the operando time for the three cycles of the cell. The horizontal blue (dashed) line represents the time at which the current polarity was switched and the red (dotted) line represents the end of a cycle. In (B) is the corresponding bicolor contour plot of the ^7Li NMR dOp spectra. Green peaks represent lithium formation (lithiation) and red peaks represent lithium removal (delithiation). In (C) is the corresponding cyclic voltammogram (black line) and the projection of the derivative plot from -200 to 160 ppm (red dashed line), and from 200 to 350 ppm (black dotted line). Peaks labeled A, B, C, D, and E depicted in the second cycle represent the formation of LiC_{36} , LiC_{27} , LiC_{18} , LiC_{12} , and LiC_6 respectively

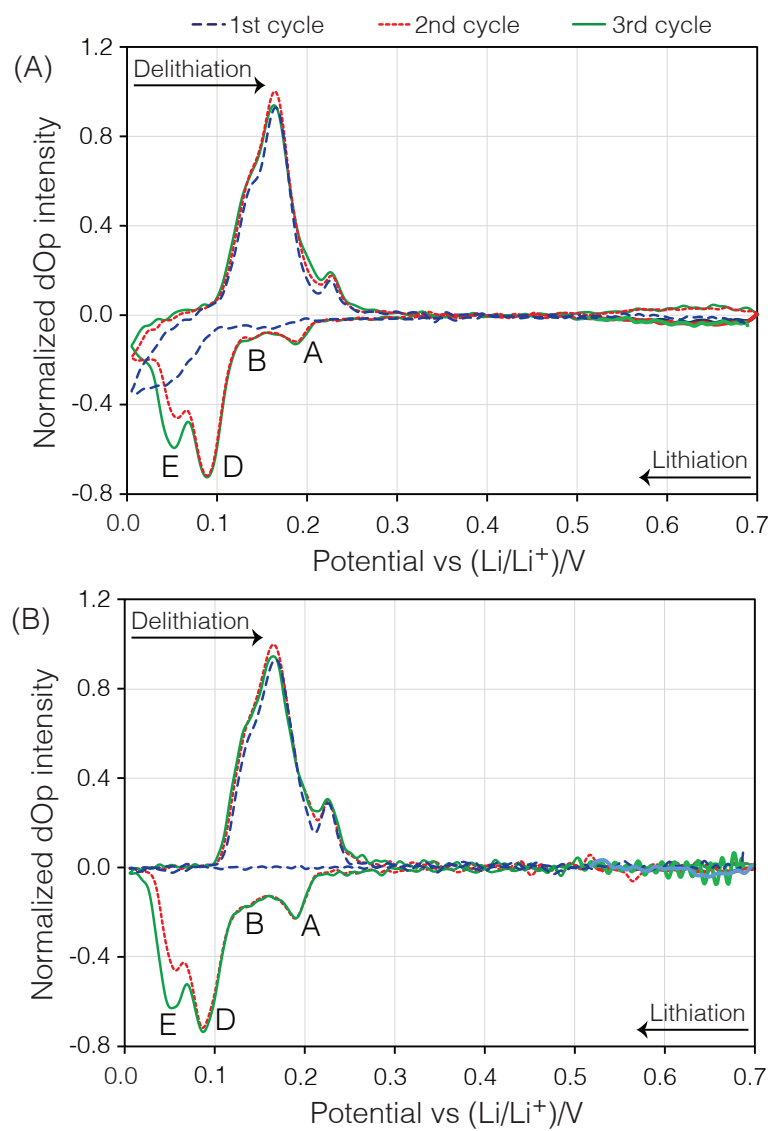


Figure S2: dOp-NMR cyclic voltammogram of the three cycles of the carbon/Li electrochemical cell taken from the projection of the ⁷Li dOp-NMR signal across (A) the graphite intercalation compounds and (B) the lithium metal. The peaks labeled as A, B, D, and E are described in the text.

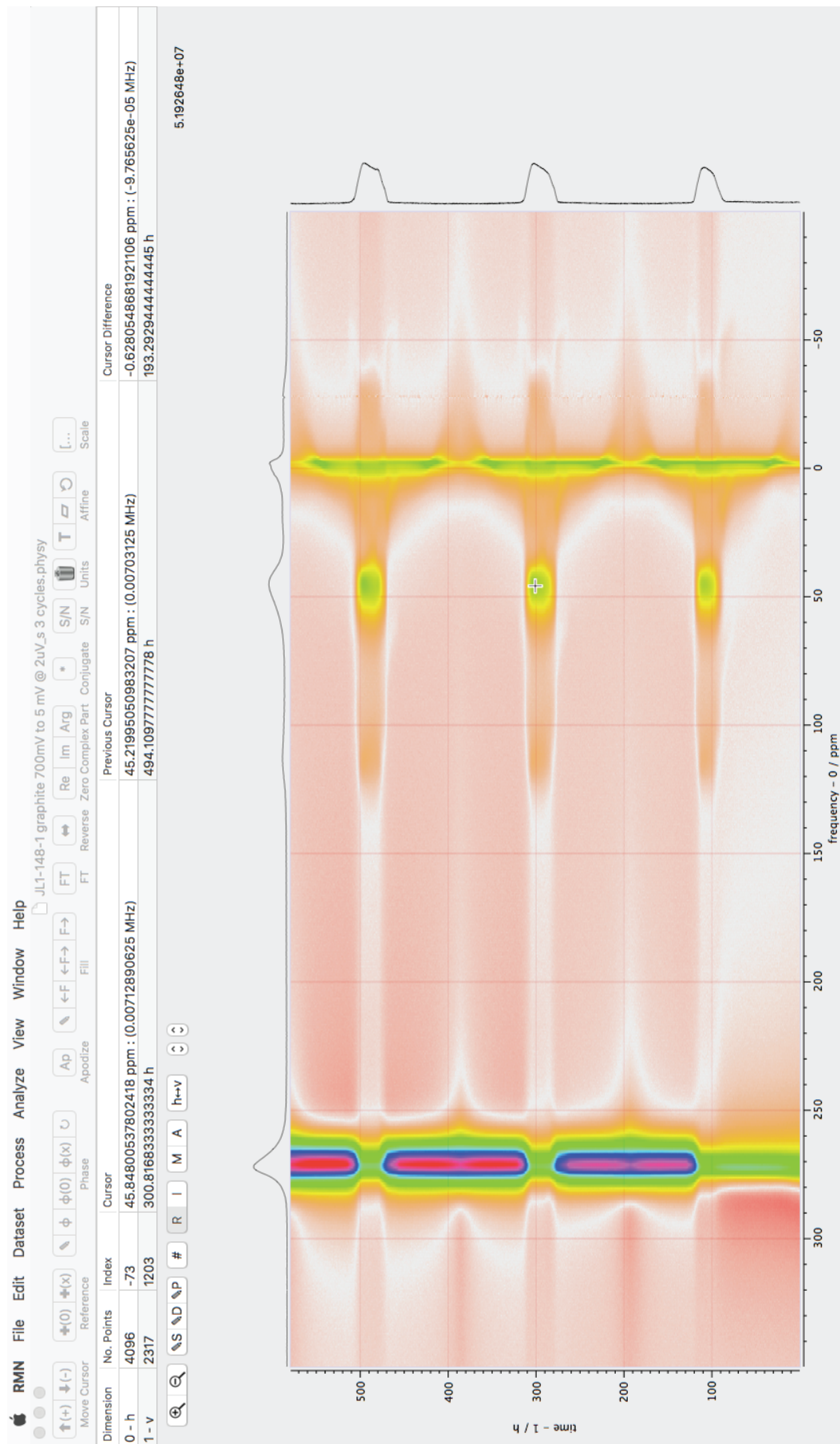
S2 Derivative Processing

Here we give a step-by-step guide to calculating the derivative of the operando signal using RMN. A similar sequence of steps can be taken in other signal processing programs such as Matlab or Mathematica. Taking a derivative through the Fourier derivative theorem consists of applying the following commands in RMN:

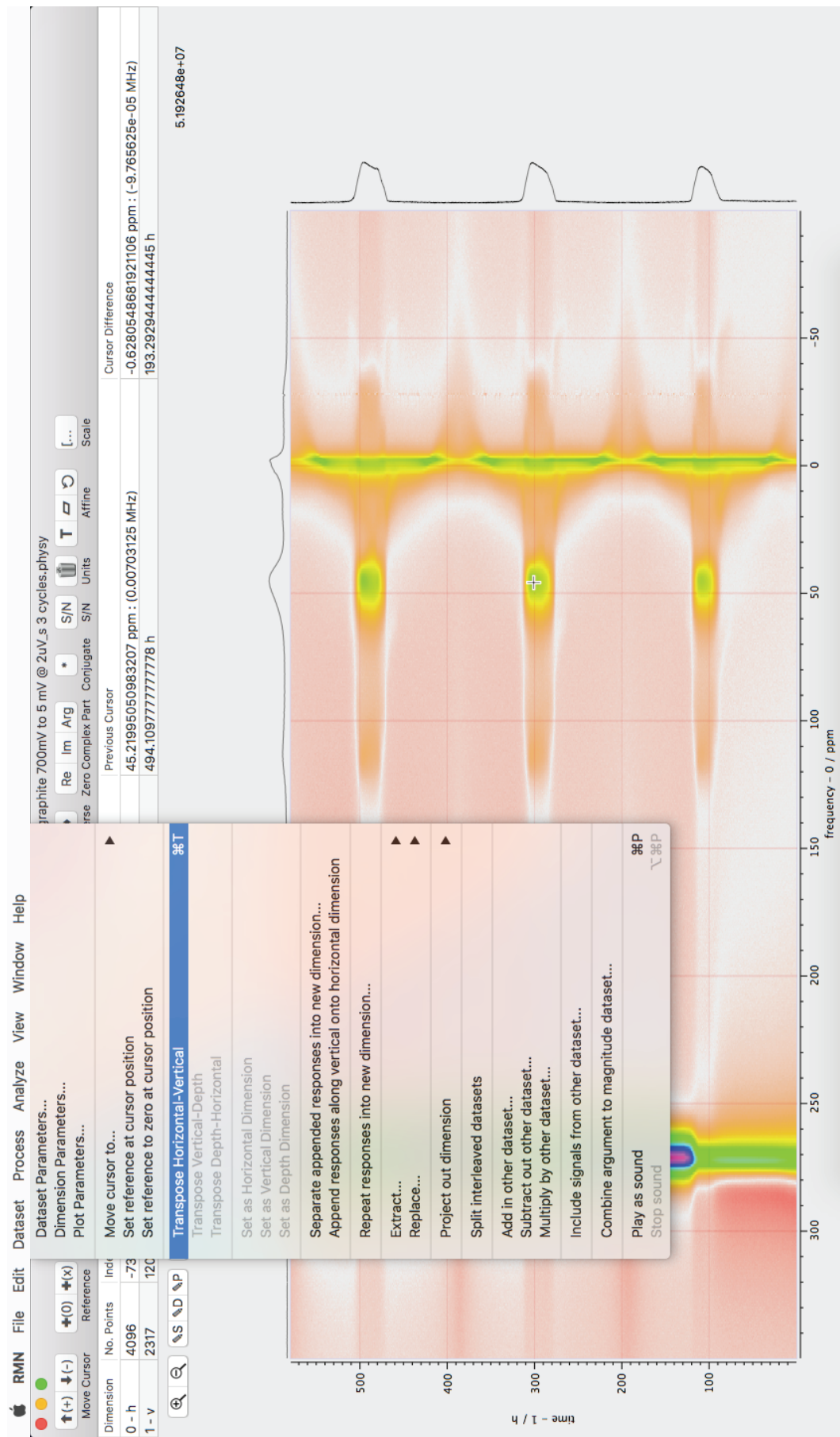
1. Fourier transforming along the operando dimension.
2. Applying the derivative convolution along the operando dimension.
3. Applying a hamming filter along the operando dimension.
4. Inverse Fourier transforming along the operando dimension.

All parameters used in processing the signal are shown.

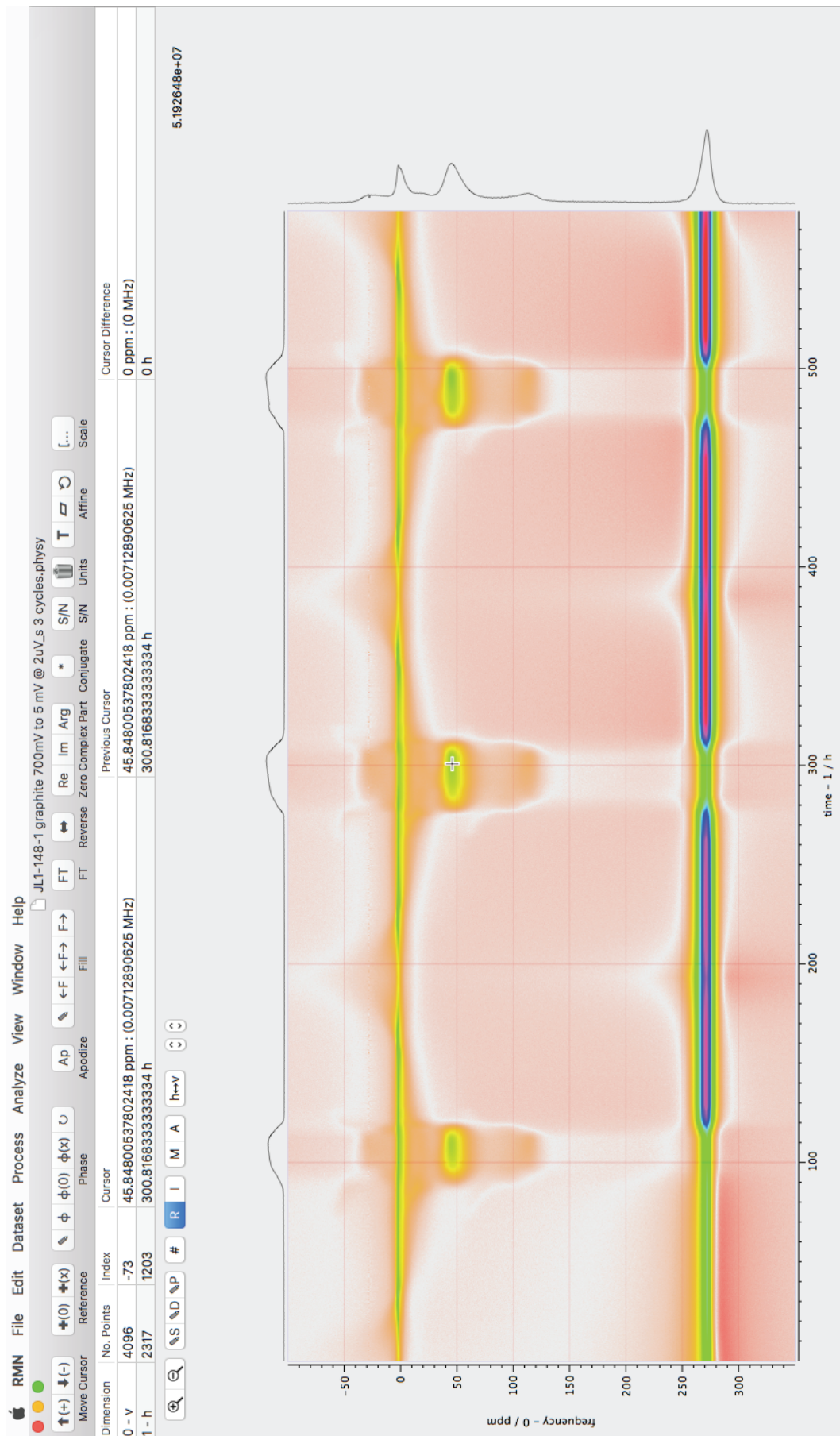
Below is a view of the Operando ^7Li NMR spectra of the three cycles of the electrochemical cell opened in RMN. The second cycle was shown in Figure 3 on the main text.



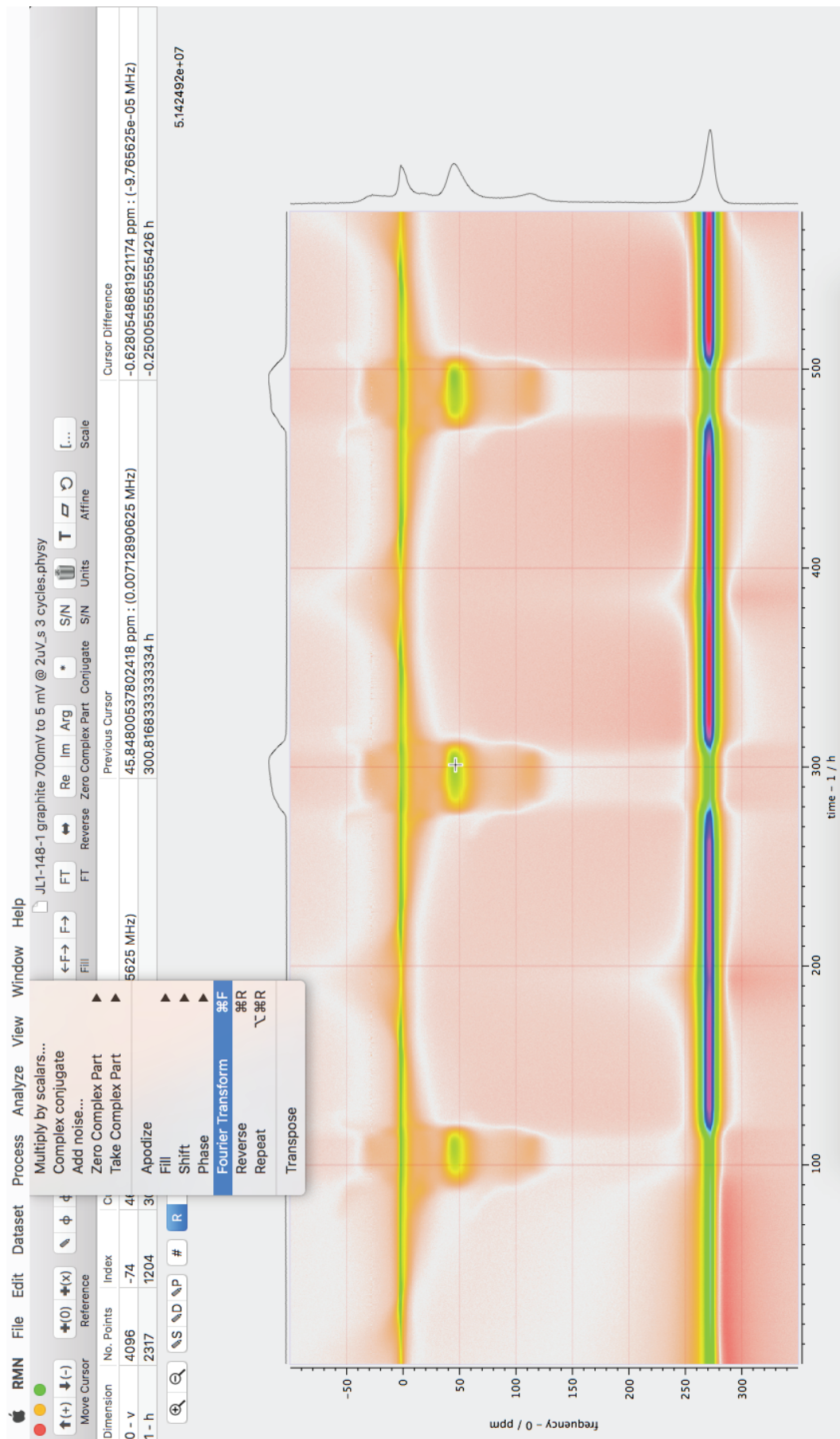
Transpose: All one-dimensional operations in RMN are applied to the signal along the horizontal dimension, therefore, before taking the derivative of the spectrum as a function of operando time, the spectrum is transposed to place the operando dimension along the horizontal. The command to transpose the horizontal and vertical dimensions in RMN are located under the “Dataset” menu.



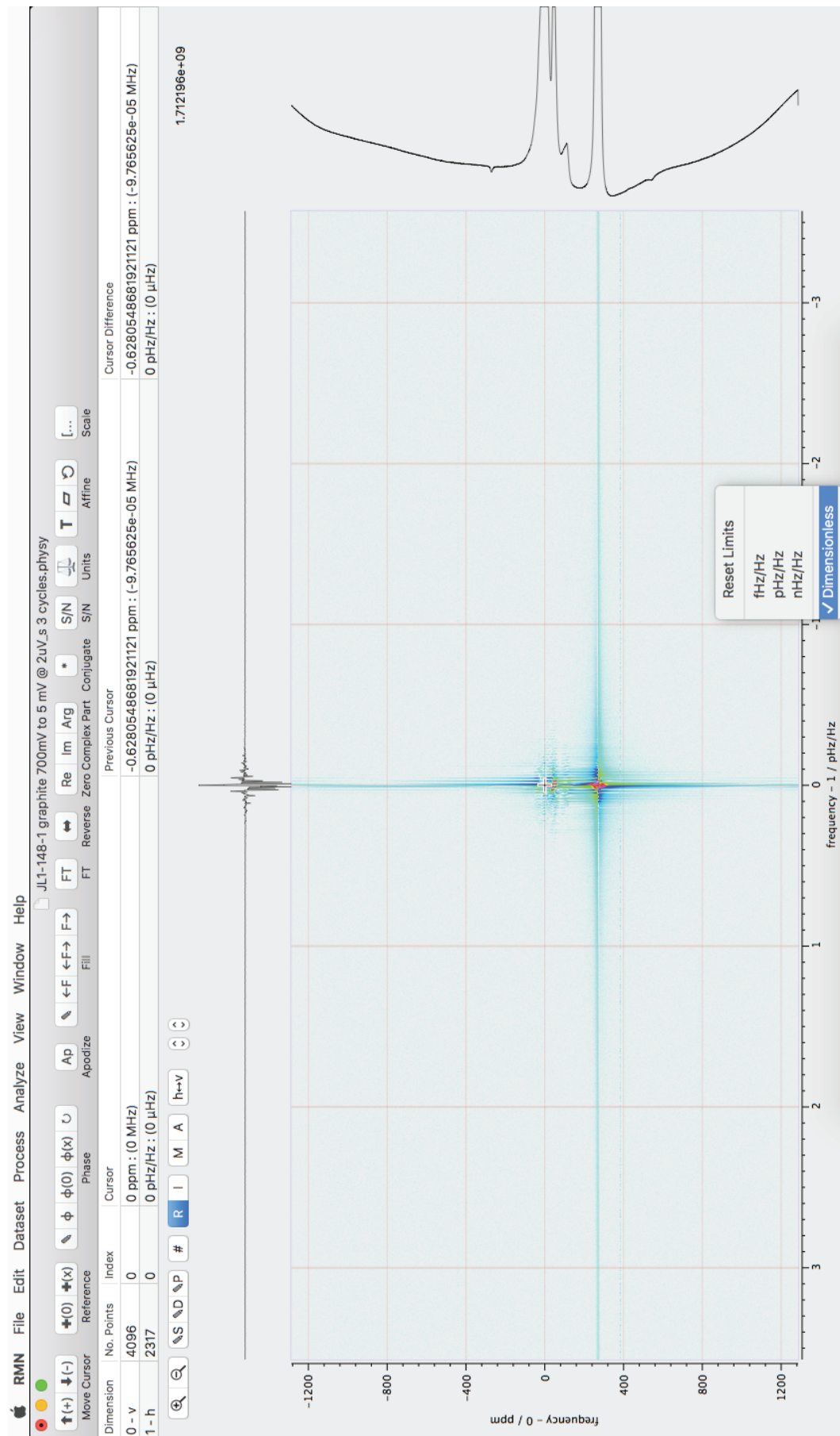
Below is the signal after transposing.



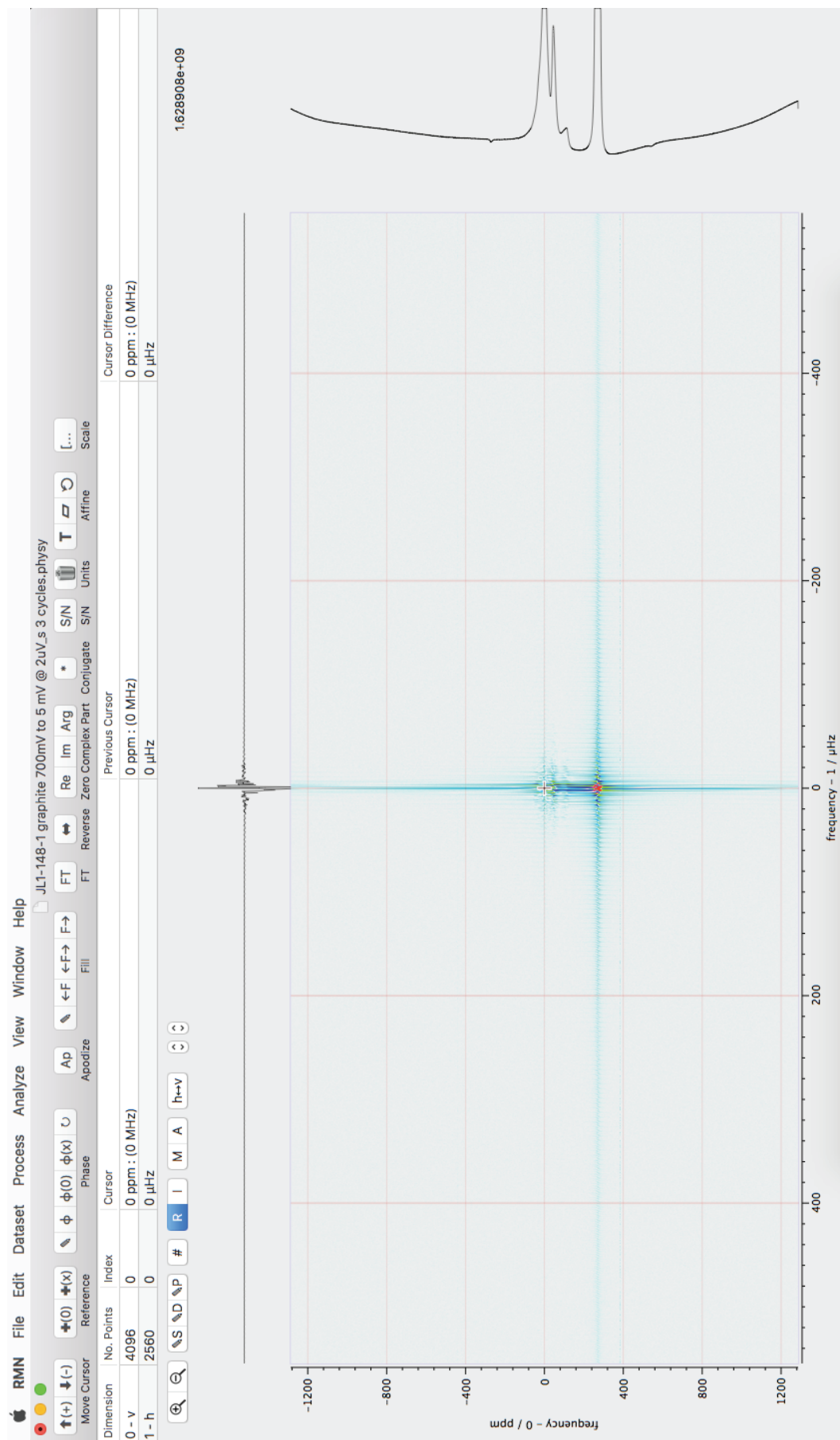
Fourier Transform: Apply a Fourier transform along the horizontal dimension to transform the operando time domain signal into a frequency domain signal. The command to “Fourier Transform” the spectra is located under the “Process” menu as shown below.



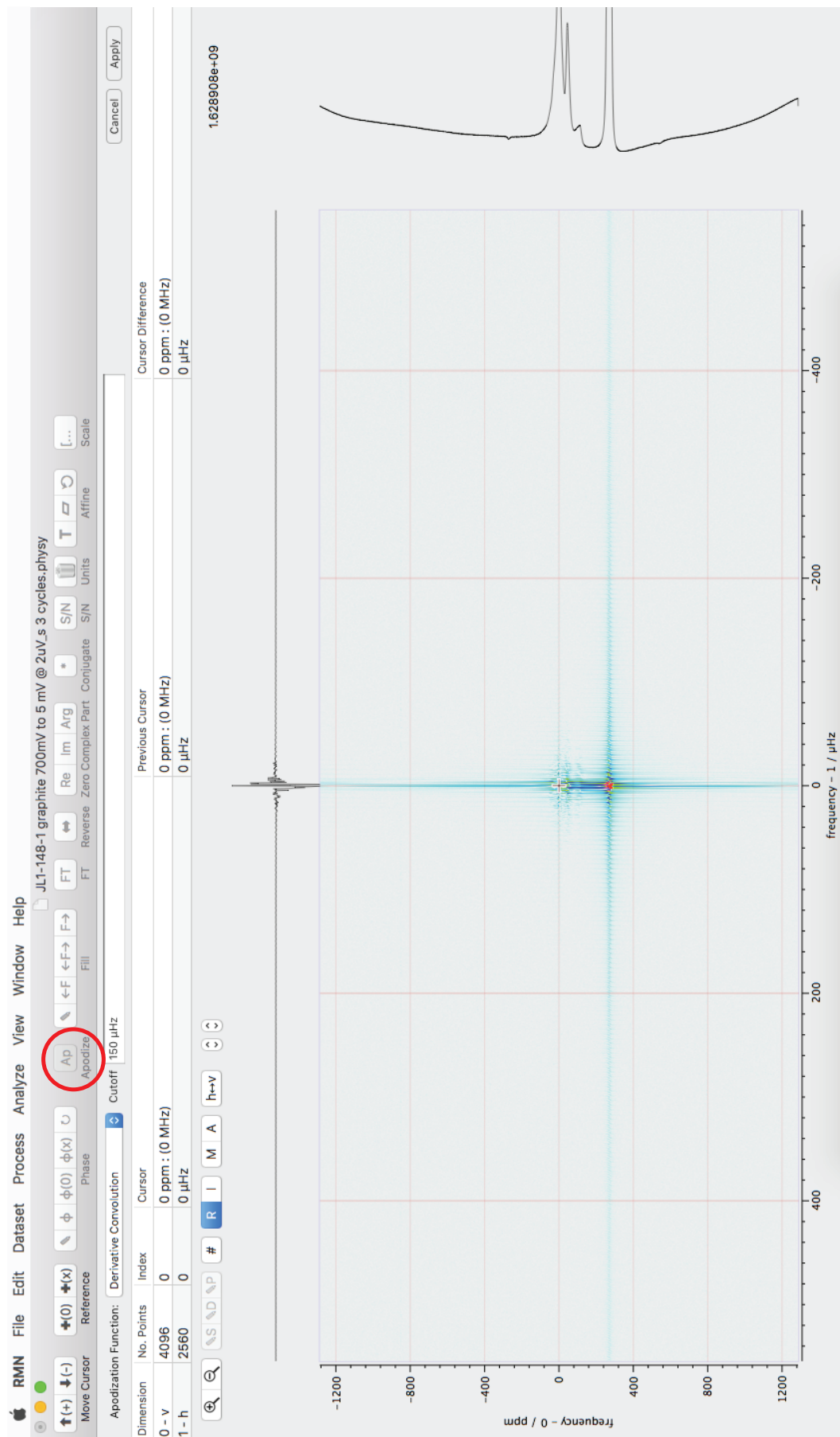
After the Fourier transform we obtain the signal below. Since RMN automatically converts the frequency domain axis of NMR signals into a dimensionless frequency ratio axis is it necessary in this case to convert the horizontal dimension back to units of frequency by clicking anywhere in the horizontal axis and unchecking the Dimensionless flag as shown below.



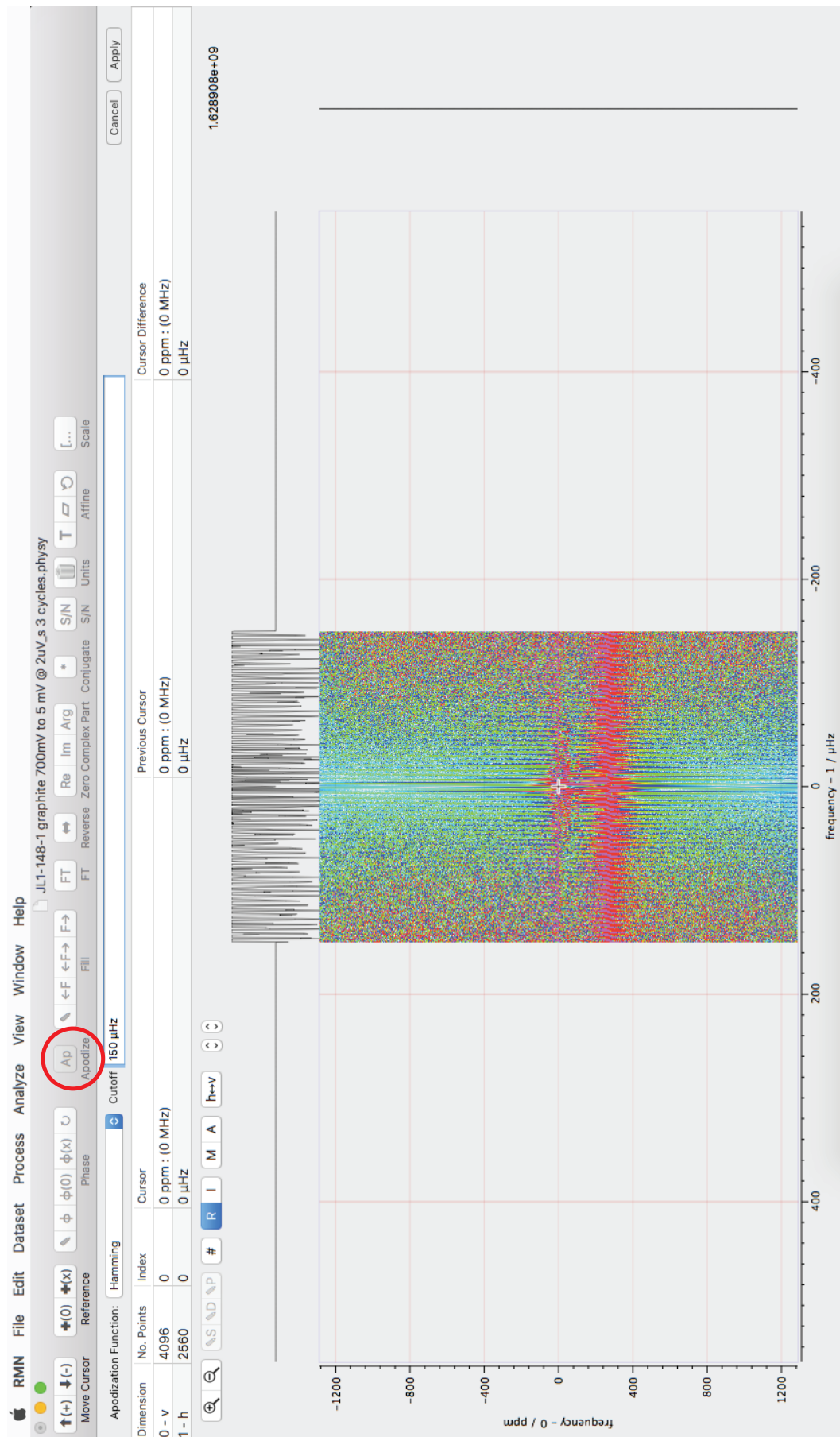
Below is the signal after the Fourier transform with the horizontal axis with units of μHz .



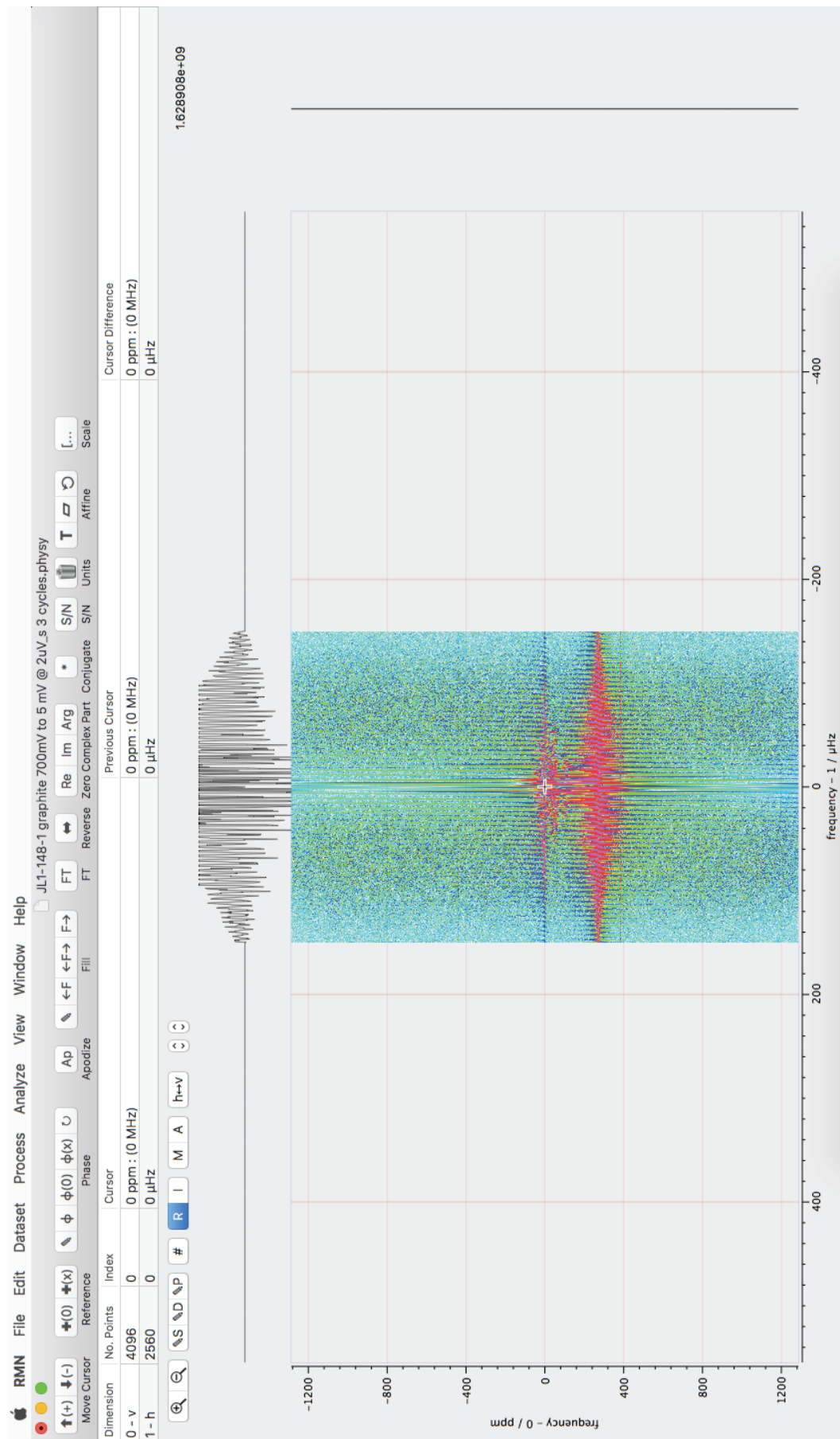
Apply Derivative Convolution: The apodization is done by clicking the Ap button (circled in red) or under the “Process” menu. This will display a dialog with a popup menu displaying available apodization functions. With the popup menu select “Derivative Convolution.” For the cutoff frequency enter a value where the spectra shows mainly noise. In this case, a cutoff frequency of 150 μHz is used. Click the Apply button on the right.



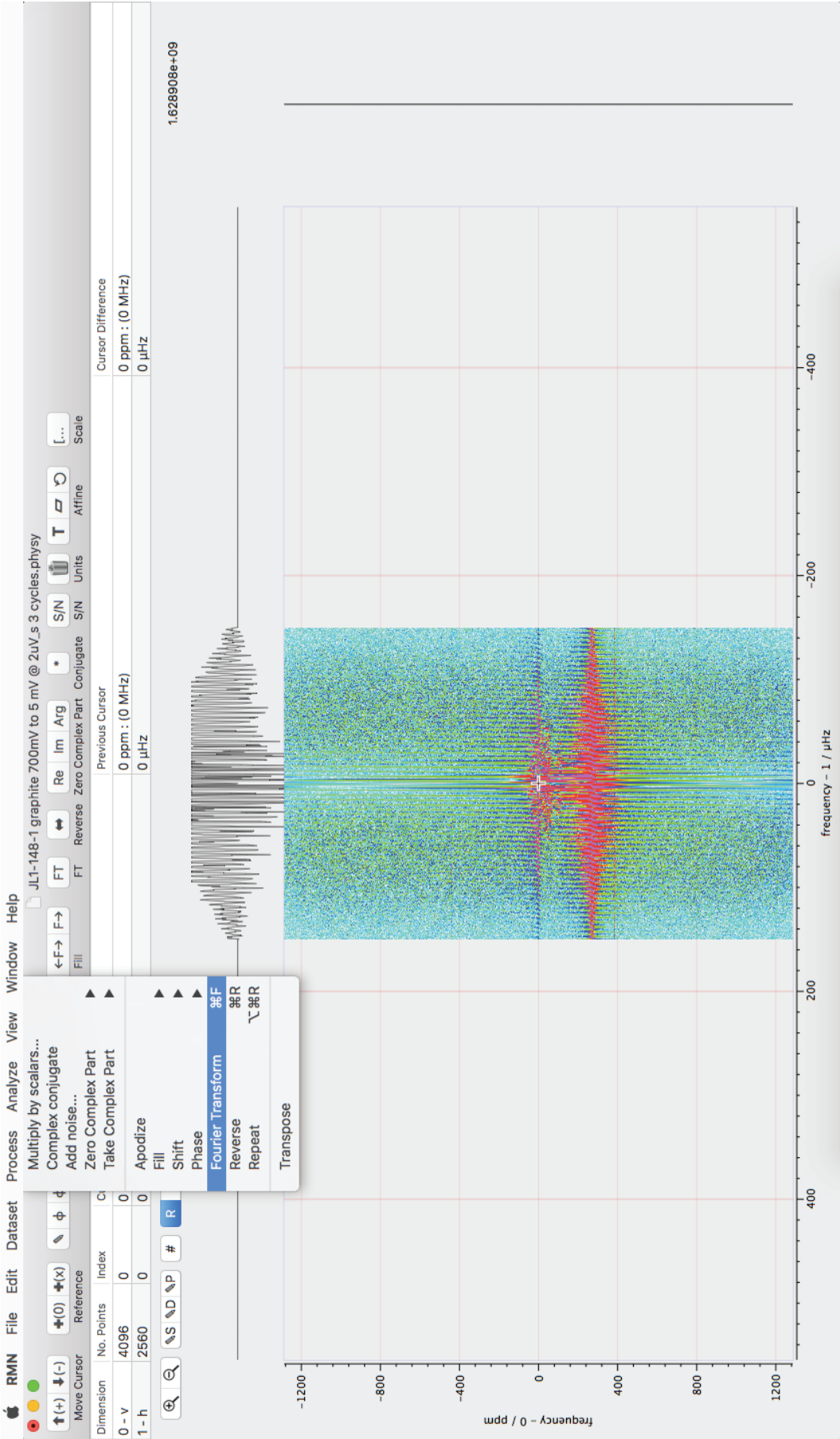
Apply Hamming Filter: To avoid artifacts from using a sharp cutoff frequency an additional hamming filter is applied using the same cutoff frequency. Select the “Hamming” apodization function is selected with the popup menu. Enter a cutoff frequency of 150 μHz , and click the Apply button.



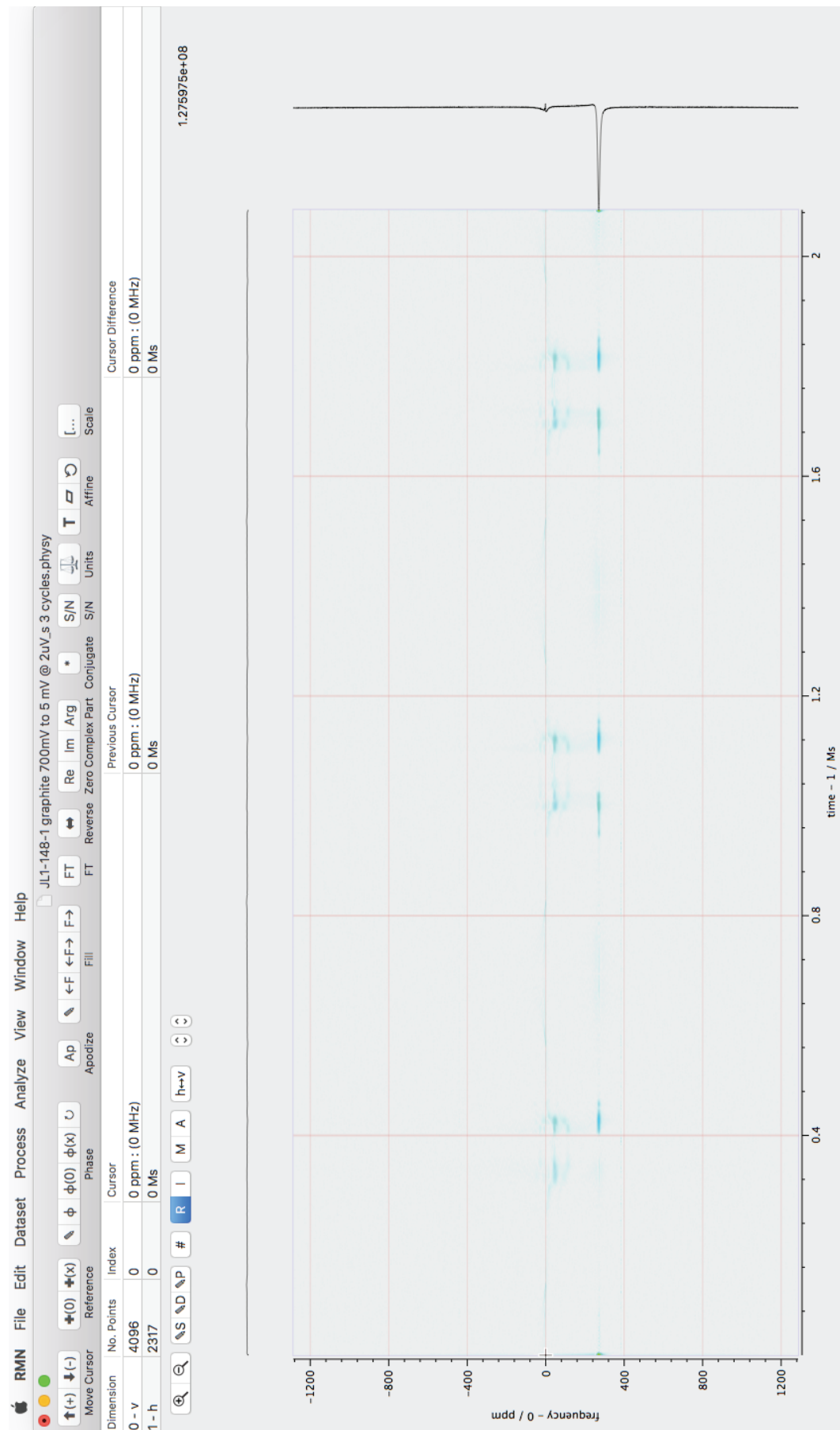
Signal after the hamming function has been applied.



Inverse Fourier Transform: An inverse Fourier transform is then applied to bring the signal back to the operando time domain along the horizontal dimension.



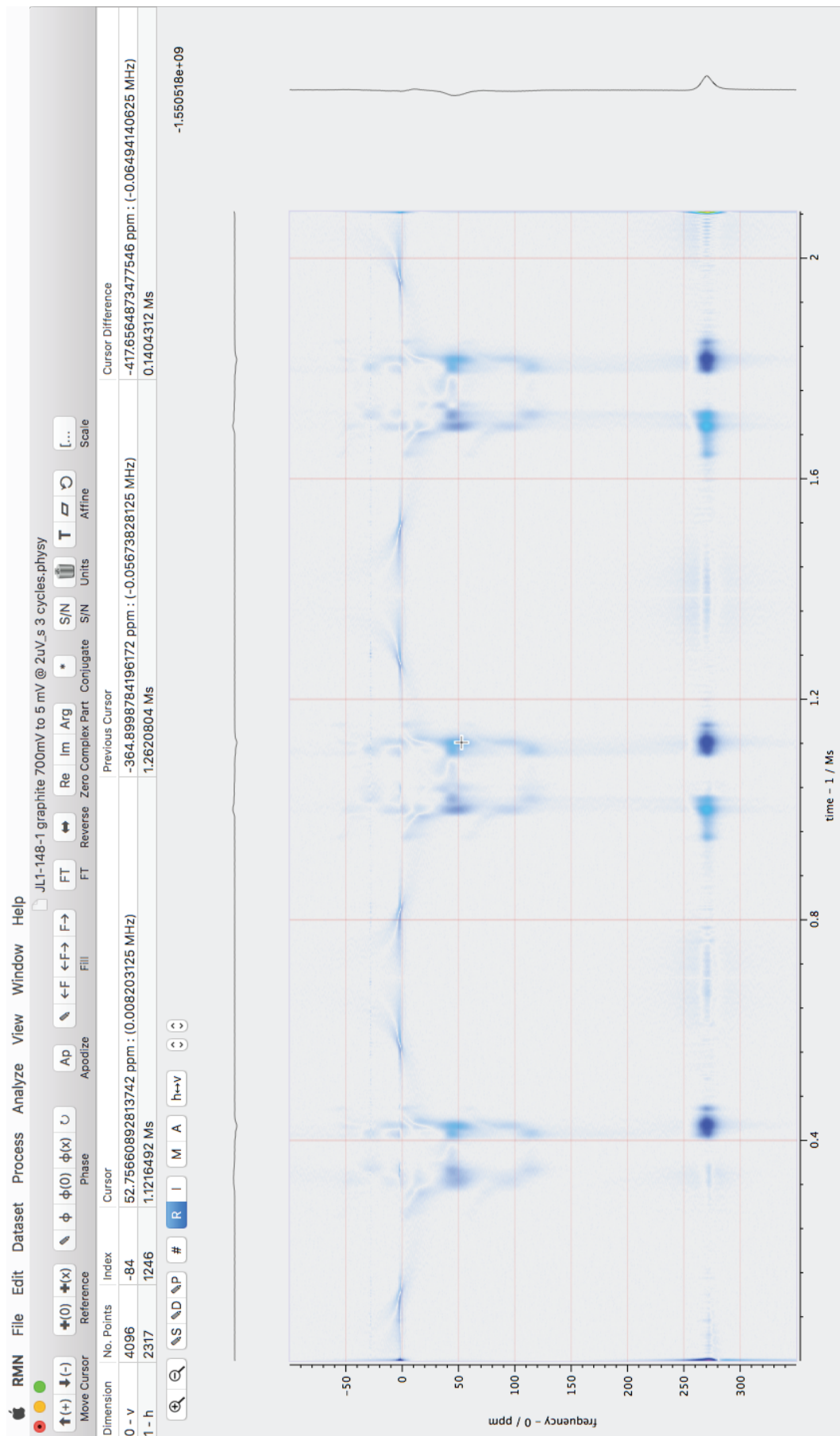
Signal after the inverse Fourier transform. The derivative along the horizontal dimension is complete and the dOp signal is obtained. In the next few steps we adjust the presentation of the signal to match the figure in the main text.



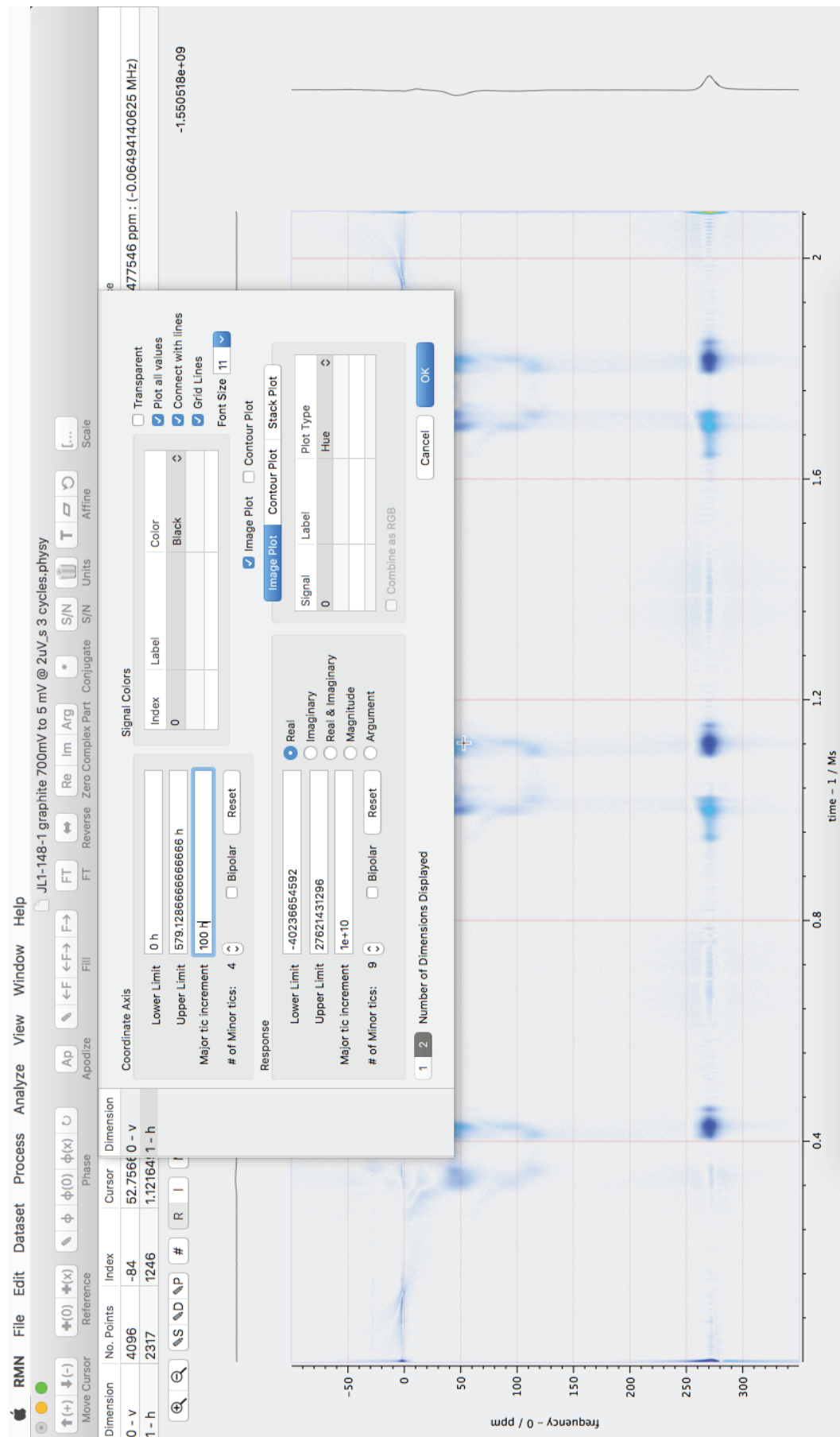
The vertical (NMR frequency) axis is zoomed to show a spectrum within the limits of -100 to 350 ppm. These parameters can be changed by clicking the P circled in red and entering the lower and upper limits for the vertical dimension.



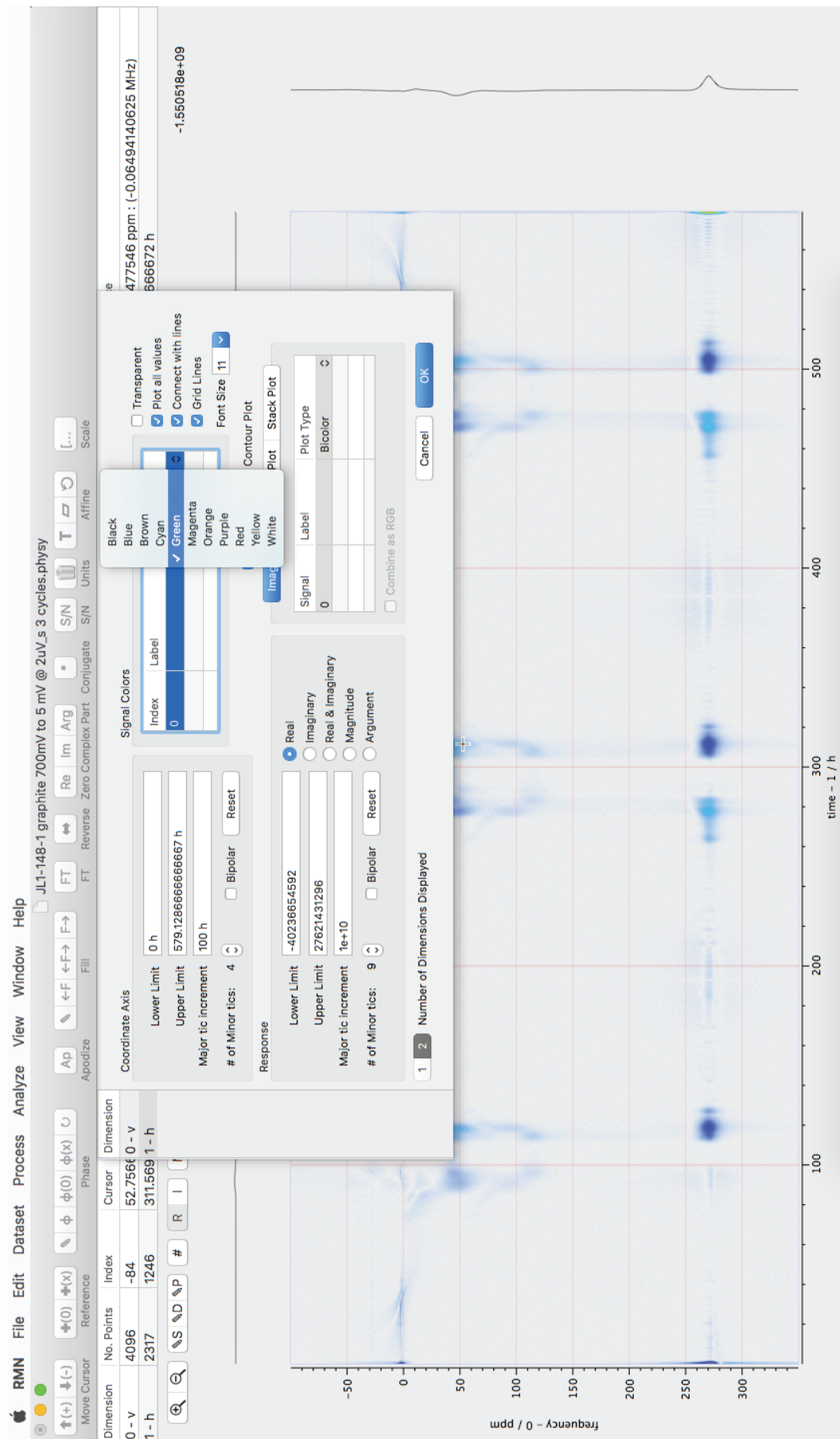
The signal after the vertical zoom.



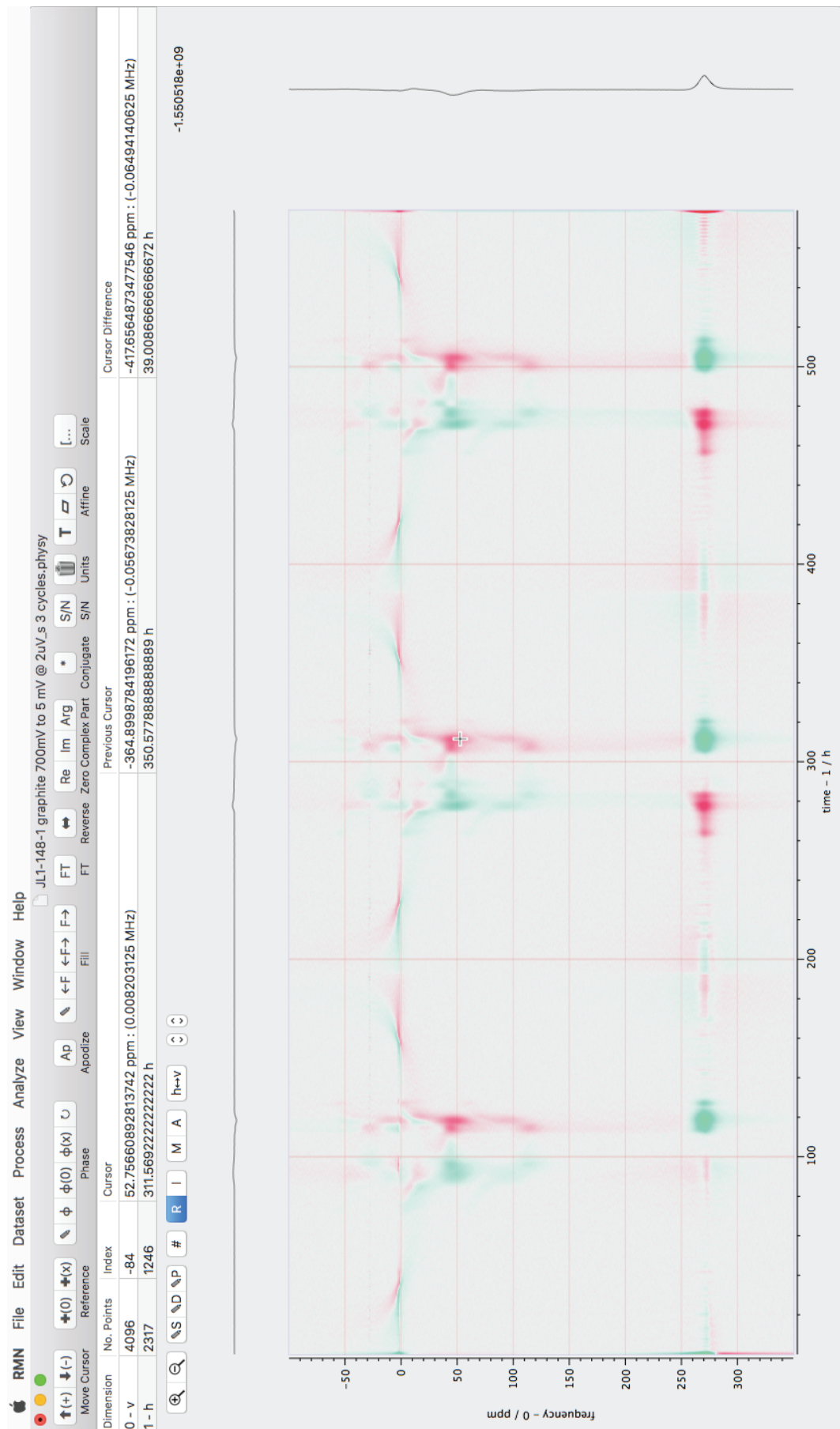
Similarly, the units of the horizontal (operando time) axis are adjusted to show the time in hours.



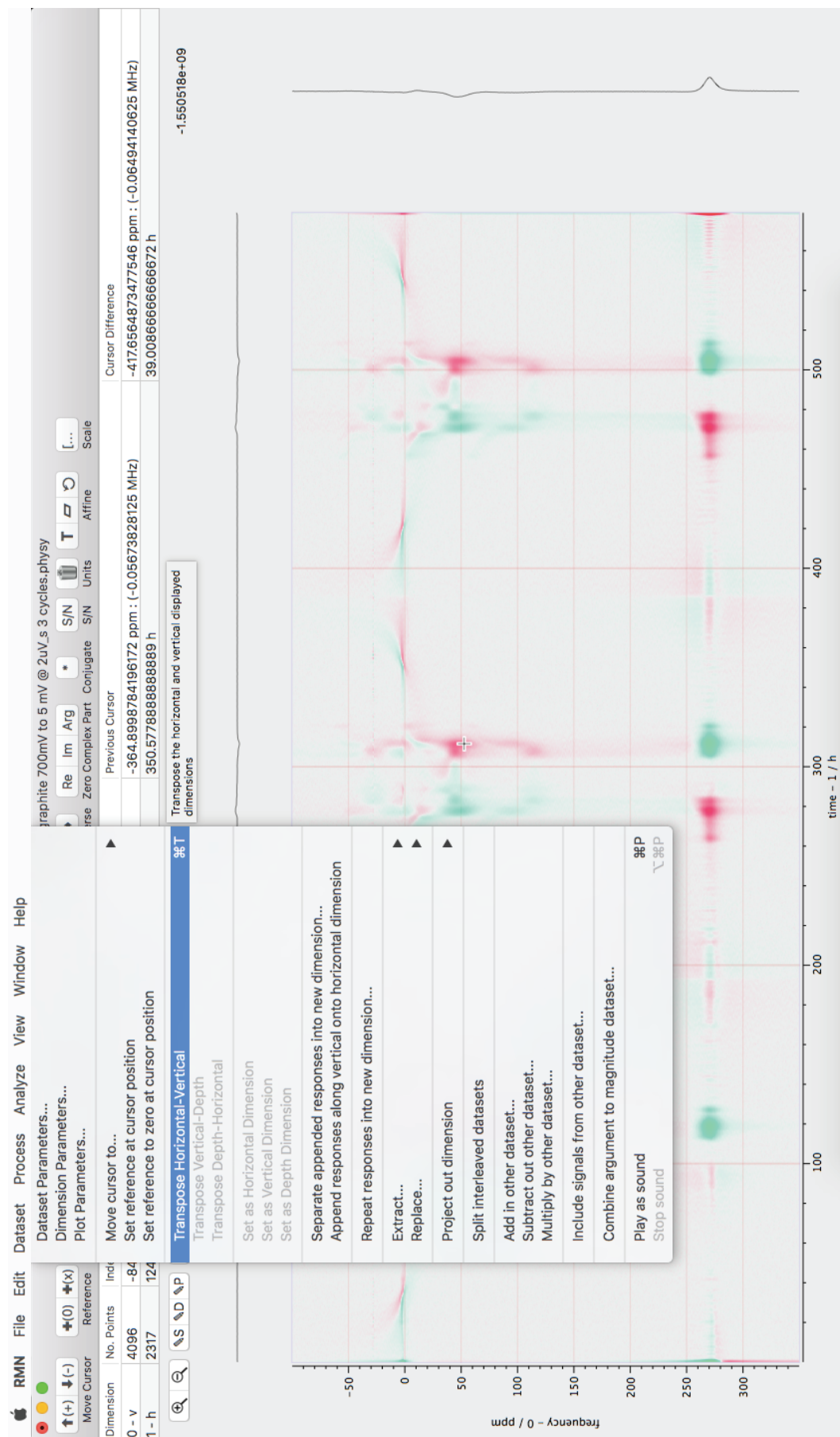
The properties of the plot are then changed to obtain a bicolor spectrum. We choose to represent positive peaks in green to represent formation of lithium species and negative going peaks in red to represent removal of lithium species.



The image below shows a bicolor dOp spectrum. Green peaks represent formation of lithium species and red peaks represent the removal of lithium species.



Next we transpose the signal to placing the NMR frequencies along the horizontal dimension and the operand time along the vertical dimension.



RMN File Edit Dataset Process Analyze View Window Help

JL1-148--1 graphite 700mV to 5 mV @ 2uV_s 3 cycles.physy

	No. Points	Index	Cursor	Previous Cursor	Cursor Difference
0 - h	4096	-72	45.21995050983207 ppm : (0.00703125 MHz)	52.75660892813742 ppm : (0.008203125 MHz)	7536658418305348 ppm : (0.00171875 MHz)
1 - v	2317	1243	310.8190555555556 h	311.5692222222222 h	0.7501686686666279 h

S D P # R I M A h+v (c) (C)

-1.849591e+09

